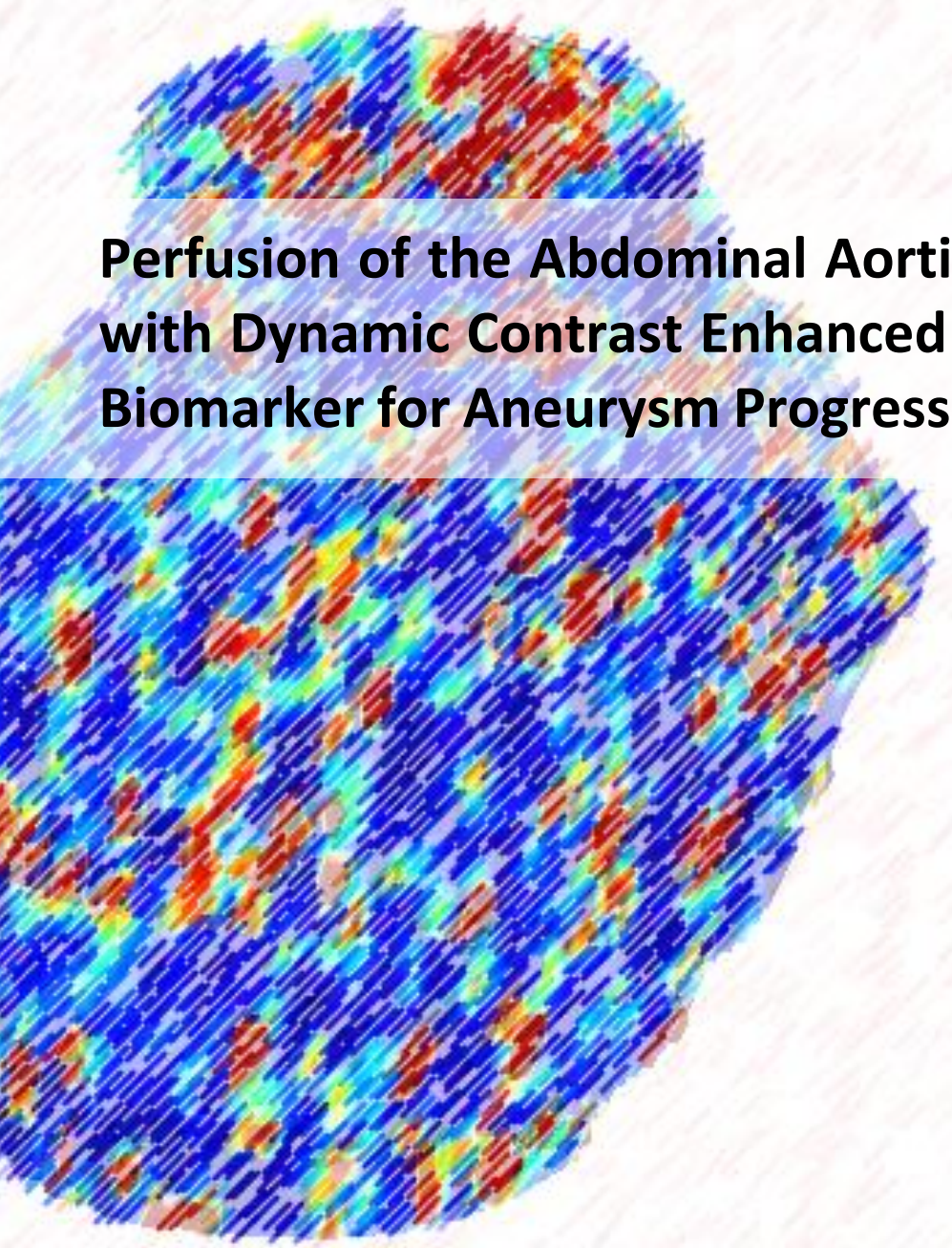

Perfusion of the Abdominal Aortic Aneurysm Wall with Dynamic Contrast Enhanced MRI; A Potential Biomarker for Aneurysm Progression and Rupture?

Lotte Rijken

Master Thesis Technical Medicine | Medical Imaging and Interventions

September 2022

UNIVERSITY OF TWENTE.

Amsterdam UMC
Universitair Medische Centra

Perfusion of the Abdominal Aortic Aneurysm Wall with Dynamic Contrast Enhanced MRI; A Potential Biomarker for Aneurysm Progression and Rupture?

Lotte Rijken
S1702777

Master Thesis Technical Medicine| Medical Imaging and Interventions
University of Twente
Amsterdam University Medical Centers Department of Vascular Surgery

Graduation Committee:

Head of committee	Prof.dr.ir. C.H. Slump
Medical supervisor	Dr. K.K. Yeung
Technical supervisor	Dr. J.M. Wolterink
Technical supervisor	Dr. O.J. Gurney-Champion
Technical Physician supervisor	Drs. S.P.M. Smorenburg
Process supervisor	Drs. A.G. Lovink
External member committee	Drs. J.A. Simmering

September 2022

Preface

Before you lies the master thesis 'Perfusion of the Abdominal Aortic Aneurysm Wall with Dynamic Contrast Enhanced MRI; A Potential Biomarker for Aneurysm Progression and Rupture?'. This thesis is the last step of my studies of Technical Medicine, which is focused on medical imaging and interventions, at the University of Twente. Over the course of the last year I have worked at the department of vascular surgery in the Amsterdam University Medical Centers to obtain clinical experience and to learn more about scientific research by writing my thesis.

This work started as a small introduction project but ended up being my full thesis project in which I investigated the calculation of perfusion maps and its clinical value. During this period, I got familiar with complex DCE-MRI techniques including post-processing steps and I was introduced to working with deep learning models. Through this I have gained more experience in programming. Furthermore, I got the opportunity to improve my scientific research skills in general.

I want to thank my supervisors for helping me writing my thesis, improving my research skills and being very approachable for all my questions. I want to thank Kakkhee for pushing me to analyze the problems from a clinical perspective and to find clinical correlations. I want to thank Jelmer for his challenging questions about the deep learning methods which strived me to learn more about them. I want to thank Oliver for all the patience and guidance to help me understand the complex processes of DCE-MRI. Stefan, thank you for helping me to look at the project from a Technical Medicine point of view and improving my writing skills. Also, I want to thank Annelies for helping me to place things in perspective and help me grow personally. Eva, Maarten and Kaj thank you for all the days at the office, for all your help during my thesis and for the fun lunch breaks. Last but not least, I want to thank my family and friends for all their help, support, patience, and being there for me.

Abstract

BACKGROUND – Nowadays, the maximal diameter is used as a measure for the treatment of abdominal aortic aneurysms (AAAs). However, the predictive value of the maximal diameter for aneurysm rupture is not always sufficient. Hence, there is a need for a better patient-individual prediction of AAA progression and risk of rupture. The perfusion of the AAA wall may be a potential biomarker. AAA wall perfusion can be measured using Dynamic Contrast Enhanced MRI (DCE-MRI) by the quantification of the volume transfer constant K_{trans}.

METHODS – 3D DCE-MRI data of twenty AAA patients were analyzed. Seventeen patients received two consecutive DCE-MRI scans at a one-week interval. Two different methods were assessed to perform pharmacokinetic modeling for generating K_{trans} maps. The conventional least squared (LSQ) fitting method was compared to a physics-informed deep learning network (DCE-net). Each method was evaluated for reproducibility of scan and rescan. Subsequently, clinical analysis of the generated 3D Ktrans maps of the aneurysm wall was performed. AAA diameter and growth per year were correlated to median and maximum K_{trans} values.

RESULTS – In total, seventeen patients underwent consecutive DCE-MRI scans and were included for further K_{trans} analysis. The K_{trans} maps were moderately reproducible in both the LSQ fitting and DCE-net methods. The coefficients of variation (CoV) of the LSQ fitting and the DCE-net for the small segments were 45.4% and 48.5%, respectively, and for large segments 24.5% and 27.3%, respectively. While comparing the small and large regions of the 3D K_{trans} maps, there was a fixed bias between scan and rescan (-0.05 min^{-1} for the LSQ fitting and -0.04 min^{-1} for the DCE-net). There was no fixed bias of median K_{trans} values of the whole AAA wall between the two scans. Clinical analysis was performed for the K_{trans} maps generated with the LSQ method. Median K_{trans} of the whole annotated AAA of the first DCE-MRI scan and the AAA diameter measured on ultrasound had a significant correlation (R=-0.51, P = 0.043). There was a moderate correlation between the 95th percentile K_{trans} value of the whole annotated AAA of the first scan and the mean growth per year (R=-0.51, P = 0.045).

CONCLUSION – In this study, K_{trans} could be quantified on 3D DCE-MRI data using the LSQ fitting and DCE-net. The DCE-net did not outperform the conventional LSQ fitting. Still, the derived parameter maps from DCE-MRI data were sensitive to acquisition and post-processing techniques. The generated 3D K_{trans} maps were more robust for larger regions compared to smaller regions. Furthermore, the clinical use of K_{trans} as a biomarker for progression and rupture could not yet be determined based on the results of this thesis.

Contents

List of Abbreviations

Abbreviation	Definition
AAA	Abdominal Aortic Aneurysm
AIF	Arterial Input Function
AP	Anterior-Posterior
CoV	Coefficient of Variation
CERRM	Constrained Extended Reference Region Model
DCE-MRI	Dynamic Contrast Enhanced MRI
DCE-net	Dynamic Contrast Enhanced MRI parameter estimation network
EES	Extravascular Extracellular Space
ETofts	Extended Tofts
EVAR	EndoVascular Aneurysm Repair
FFE	Fast Field Echo
GRU	Gated Recurrent Unit
iMSDE	improved Motion-Sensitized Driven-Equilibrium
k_{ep}	Efflux rate constant
K_{trans}	Volume transfer constant
LSQ	Least SQuares
LSTM	Long Short-Term Memory
MARVY	MRI-based endovasculAR procedures for Vascular surgery
PK	Pharmacokinetic
ROI	Region Of Interest
T1 relaxation	Longitudinal relaxation
T10 relaxation	Pre-contrast longitudinal relaxation
T2 relaxation	Transverse relaxation
T20 relaxation	Pre-contrast transverse relaxation
TFE	Turbo Field Echo
TR	Repetition Time
UMC	University Medical Centers
v_e	Fractional volume of extravascular extracellular space
v_p	Fractional volume of blood plasma

1 Introduction

An abdominal aortic aneurysm (AAA) is a pathological dilatation of the abdominal aorta that can be life-threatening since it can lead to aortic rupture. Without treatment, patients with ruptured AAAs will die and even if ruptured AAAs are treated the 30-day mortality rate is still 13-53%. Therefore, it is of major importance to prevent rupture of an aneurysm and to perform elective treatment. (1)

However, prediction of aneurysm progression and rupture is not straightforward. For years, the maximum AAA diameter is used as a measure for the decision of performing elective treatment. Although, currently used guidelines for elective AAA intervention, which are an AAA diameter >5.5 cm for men and >5.0 cm for women, or >1 cm/year growth, do not always apply since small AAAs can still rupture and large AAAs may not rupture. Consequently, there is a need for better patient-individual prediction of AAA progression and risk of rupture. (1, 2)

Functional imaging biomarkers may be used to guide clinical decision making for AAA treatment. These biomarkers can provide information about the functional status of the AAA wall and are promising measures for the prediction of progression and rupture for individual patients. Examples of potential functional biomarkers are blood flow, peak wall stress, wall shear stress, intraluminal thrombus, and the microvascularization of the AAA wall, which can be measured on MRI. (3)

One of the potential biomarkers for disease progression and AAA rupture measured on MRI is the perfusion of the aortic wall. Dynamic contrast enhanced (DCE) MRI is able to quantify perfusion by calculation of the volume transfer constant (K_{trans}) (4). Nguyen et al. (5) describe that a high K_{trans} of the aortic wall, meaning a high blood flow, large surface area and high permeability of microvessels, may indicate that the vessel wall is more likely to weaken. Therefore, K_{trans} may be a potential biomarker for AAA progression or rupture to better quantify whether and when a patient requires surgical treatment.

Nguyen et al. (5) have assessed the feasibility and reproducibility of K_{trans} quantification by two-dimensional single-slice acquisition DCE-MRI and were able to quantify the microvasculature of the AAA vessel wall in several slices. However, 3D imaging of the AAA wall has the preference over 2D imaging to obtain a perfusion map of the complete AAA wall instead of being limited to single slices. Wang et al. (6) have developed a 3D DCE-MRI protocol to quantify K_{trans} in carotid vessel walls. 3D quantification of K_{trans} for the aortic vessel wall has not been performed yet. Before K_{trans} of the AAA wall can be used as a biomarker in clinical practice, 3D DCE-MRI still faces technical difficulties that need to be solved to improve the accuracy of the quantification of K_{trans} (6). Furthermore, the clinical value of K_{trans} as a potential biomarker for AAA progression and rupture risk needs to be assessed.

2 Background

2.1 Clinical

2.1.1 Abdominal aortic aneurysms

An AAA is generally defined as a dilated abdominal aorta with a diameter of ≥30 mm (1). The overall incidence of AAAs is 1-3%, but the incidence for males between 60-80 years is higher with 2.2-8.1% (7). Smoking is a large risk factor amongst other risk factors such as atherosclerosis, hypertension, ethnicity and family history of AAAs (8).

There are several types of AAAs (Figure 1). The majority (~80%) of AAAs are infrarenal aneurysms which are located below the renal arteries and have an infrarenal neck (9). In juxtarenal AAAs, the dilatation starts just below the renal arteries but does not involve the renal arteries. Pararenal AAAs include (one of) the renal arteries. Suprarenal AAAs include the renal arteries, superior mesenteric artery and/or coeliac trunk. (10)

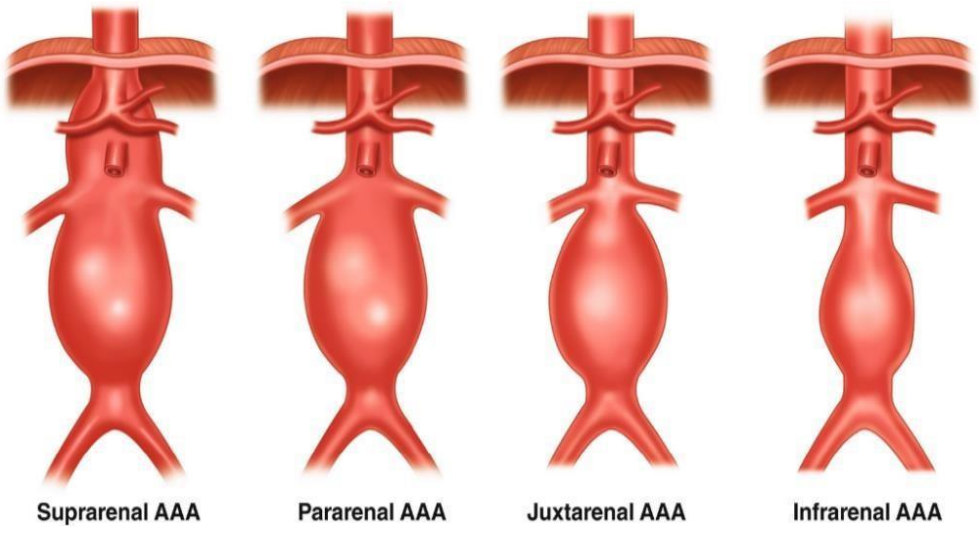

Figure 1. Illustration of different types of abdominal aortic aneurysms; suprarenal, pararenal, juxtarenal and infrarenal aneurysms. (11)

AAAs remain asymptomatic in most cases and are generally detected during other physical examinations. An asymptomatic AAA is treated when the risk of rupture is higher than the risk of surgical treatment. (1, 8) Guidelines currently advise surgery on aneurysms with a diameter >5.5 cm for males and >5.0 cm for females, or when the AAA is growing >1 cm/year (1, 12). The chance of AAA rupture will increase above the surgical guideline thresholds. However, the risk of rupture is still patient-dependent and individual variations remain since small AAAs can still rupture and large AAAs may not rupture. (2) In case of a ruptured AAA acute treatment is necessary. (1)

2.1.2 Current AAA management

A rupture of an AAA should be prevented if possible. Therefore, patients with an AAA are being carefully observed to evaluate growth of the aneurysm. Following AAA diameter surveillance, a wait-and-see policy is applied in case the thresholds for intervention are not met or when the patient's health condition seems too poor to undergo AAA repair. When the patient is found eligible for repair, elective treatment of the AAA can be performed. Moreover, the choice of treatment is made after multidisciplinary meetings and shared decision-making with the patient. (1)

Patients can receive open surgical repair or endovascular aneurysm repair (EVAR) to repair the AAA. During an open procedure the aorta is clamped to exclude the AAA from blood flow. Subsequently, a synthetic graft is sutured to the healthy part of the aorta via end-to-end anastomosis in order to bypass the dilatated aorta. EVAR is a minimally invasive procedure whereby a stent graft is placed inside the affected part of the aorta to exclude the aneurysm from blood flow. The stent graft is inserted via a small opening in the femoral artery with use of X-ray fluoroscopy. (1) Advantages of the endovascular approach are better perioperative survival, a shorter hospital stay and shorter recovery time. However, the long-term effects and survival are not considerably better compared to open repair. (1, 13, 14)

The most suitable type of repair depends on the morphology of the aneurysm and aorta, and the patient's health condition, life expectancy, and preference for treatment. Open surgical repair is generally preferred in younger patients with a life expectancy of >10-15 years because of limited durability of EVAR stent grafts. (1) For infrarenal aneurysms a standard EVAR procedure can generally be performed whereby a stent graft is deployed directly below the renal arteries to obtain 10-15mm proximal aortic sealing against the healthy aortic wall. However, for complex aneurysms (defined as juxtarenal, pararenal and suprarenal aneurysms) the standard EVAR procedure is not sufficient in most cases due to limited infrarenal sealing of the stent graft. (15) In complex cases mostly fenestrated or branched EVAR are performed. These stent grafts include side branches to all necessary side vessels. (1)

A disadvantage of endovascular procedures in comparison to open procedures is the higher rate of postoperative complications. The most common complications after an EVAR procedure are endoleaks. (16) Endoleaks are characterized by persistent blood flow within the aneurysm sac following an EVAR procedure. Consequently, the aneurysm sac is pressurized which may cause further dilation of the aneurysm and eventually cause rupture. Endoleaks can have several causes and are categorized into the following groups:

1) Type I endoleak: leak at attachment site; type Ia is a proximal leak, type Ib is a distal leak
2) Type II endoleak: retrograde flow from covered vessels such as the inferior mesenteric artery
3) Type III endoleak: graft defect
4) Type IV endoleak: porosity of graft fabric
5) Type V endoleak: endotension; a continued expansion of the aneurysm without evidence of a leak

However, not all endoleaks have clinical significance and do require intervention. (17, 18) Type II endoleaks are the most common endoleak but generally cause a relatively low pressure in the aneurysm sac. Moreover, up to 80% of type II endoleaks resolve spontaneously over time (18). Type I endoleaks occur less frequently but result in a high pressure in the aneurysm sac (mainly Ia) and often require re-intervention. (18, 19)

2.2 Technical

2.2.1 MRI

MRI may offer benefits in the treatment of AAAs since MRI techniques can quantify physiological and functional parameters of the aneurysm. (20) In essence, MRI is an ionization-free imaging technique that

uses a strong magnetic field and the magnetic properties of protons. All protons in the human body contribute to a net magnetization and align with the main static magnetic field of the MRI scanner. When radiofrequency pulses or gradients are applied, the protons perpendicular to the main magnetic field will be tipped over. Subsequently, after switching off the radiofrequency pulse or gradients, the protons will realign with the main magnetic field and produce an electromagnetic signal in this process. Each tissue will emit a different amount of signal that will be detected with receiving coils and processed to create an image. (20, 21) Figure 2 shows an illustration of all parts of an MRI scanner including the magnets that produce the magnetic field, the gradient coils and radiofrequency coils that excide the protons, the bore and table where the patient lies. During imaging, the receiving coils are placed on the patient's body.

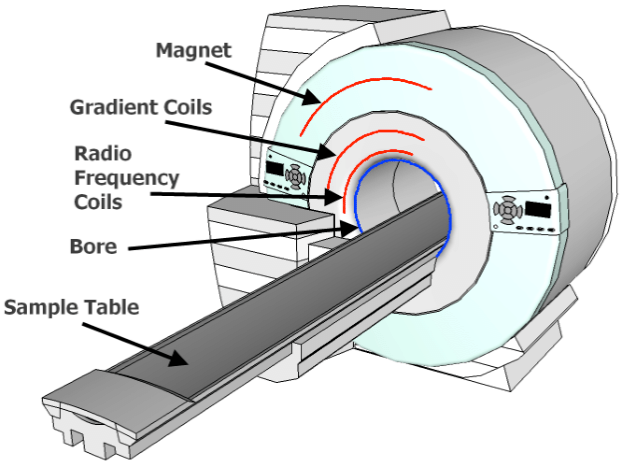

Figure 2. Illustration of MRI scanner including; magnets that produce the magnetic field, gradient coils and radiofrequency coils that excite the protons, bore, and table where the patient lies. (22)

The preoperative phase is one of the phases in AAA imaging whereby MRI can provide important functional information in addition to anatomical information. Biomarkers measured on quantitative MRI may be used to guide clinical decision-making for a better patient-specific prediction of AAA progression and risk of rupture (1, 2).

Some potential MRI biomarkers to predict AAA progression and rupture are the blood flow, peak wall stress, wall shear stress, intraluminal thrombus, and the microvascularization of the AAA wall. 4D flow MRI can quantify potential hemodynamic biomarkers such as the wall stress (23). Also, MRI has good soft tissue contrast to examine the amount of intraluminal thrombus (3). DCE-MRI can be used to quantify the microvasculature of the aortic wall (5). All these parameters can be evaluated and could potentially be biomarkers for the progression and rupture of AAAs. However, in current clinical practice, there are no MRI-derived biomarkers implemented for AAA staging because some techniques need more development and clinical evidence is lacking. (3)

2.2.2 DCE-MRI

One of the potential biomarkers for disease progression and AAA rupture measured on MRI is the perfusion status of the aortic wall. Holmes et al. (24) found that microvascularization was significantly increased in AAAs as compared to healthy aortas. Their hypothetical explanation was that high wall shear stress and ischemic injury could lead to the release of proangiogenic factors that stimulate microvascularization (24). Thereafter, increased microvascularization might weaken the aortic wall by an increase of inflammatory cells and metalloproteinases which can induce extracellular matrix remodeling (5, 25). Furthermore, a recent histopathological analysis of Bruijn et al. (26) demonstrated an increased mircrovascularisation in the AAA

wall as well. They hypothesized that localized hypoxia can be induced by intraluminal thrombus and leads to increased microvascularization and vascular wall weakening. (26, 27) In previously reported literature, the correlation between the microvascular status and risk of AAA rupture is not yet described. To quantify the perfusion of the aortic wall, DCE-MRI is able to quantify the volume transfer constant K_{trans}.

DCE-MRI is a quantitative MRI technique that can extract functional information regarding tissue perfusion and microvascular status. This MRI technique visualizes the temporal enhancement of tissues after injection of a paramagnetic contrast agent. As a result, the signal will change during injection of contrast depending on the tissue characteristics and vascularization. By analyzing this change in signal intensity, maps of four microvascular parameters can be derived (Figure 3). The parameters that can be obtained are the volume transfer constant of the contrast between blood plasma and the tissue extravascular extracellular space (EES) which is K_{trans}, the fractional volume of the EES (v_e), the fractional volume of blood plasma (v_p), and the rate constant for contrast reflux from the EES back into the blood plasma (k_{ep}). (28, 29)

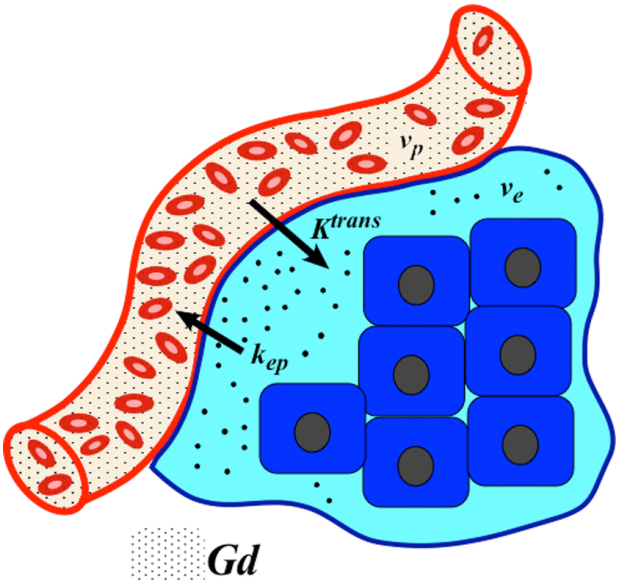

Figure 3. Schematic model of all physiological parameters that can be derived with Dynamic Contrast Enhancement MRI. The perfusion of contrast agent Gadolinium is visualized by black dots. In red the blood vessel with erythrocytes and extravascular extracellular space (EES) in blue. The physiological parameters are; the volume transfer constant of the contrast between blood plasma and the tissue EES (K_{trans}) which is important for the microvascular status of the vessel wall, the fractional volume of the EES (v_e), the fractional volume of blood plasma (v_p), and the rate constant for gadolinium reflux from the EES back into the blood plasma (k_{ep}). (28)

In DCE-MRI, a baseline scan without contrast is followed by the injection of a paramagnetic contrast agent. As a result, the MR signal intensity time curve of each voxel reflects the tissue's response to the arrival of contrast and will return to baseline when the contrast has passed. (29, 30) To quantify the microvascular biomarkers the signal time curve needs to be converted to a concentration time curve. The concentration time curve of each voxel can be fitted by performing pharmacokinetic (PK) modeling. Parametric fitting involves finding parameters for the PK model that will be fitted to the DCE-MRI data. Consequently, parameter maps of the fitting parameter K_{trans}, which represent the microvascularization of the AAA wall, can be quantified. (29, 31)

In Figure 4 the steps to obtain K_{trans} parameter maps from DCE-MRI images are illustrated. In the following sections, all steps will be explained in more detail.

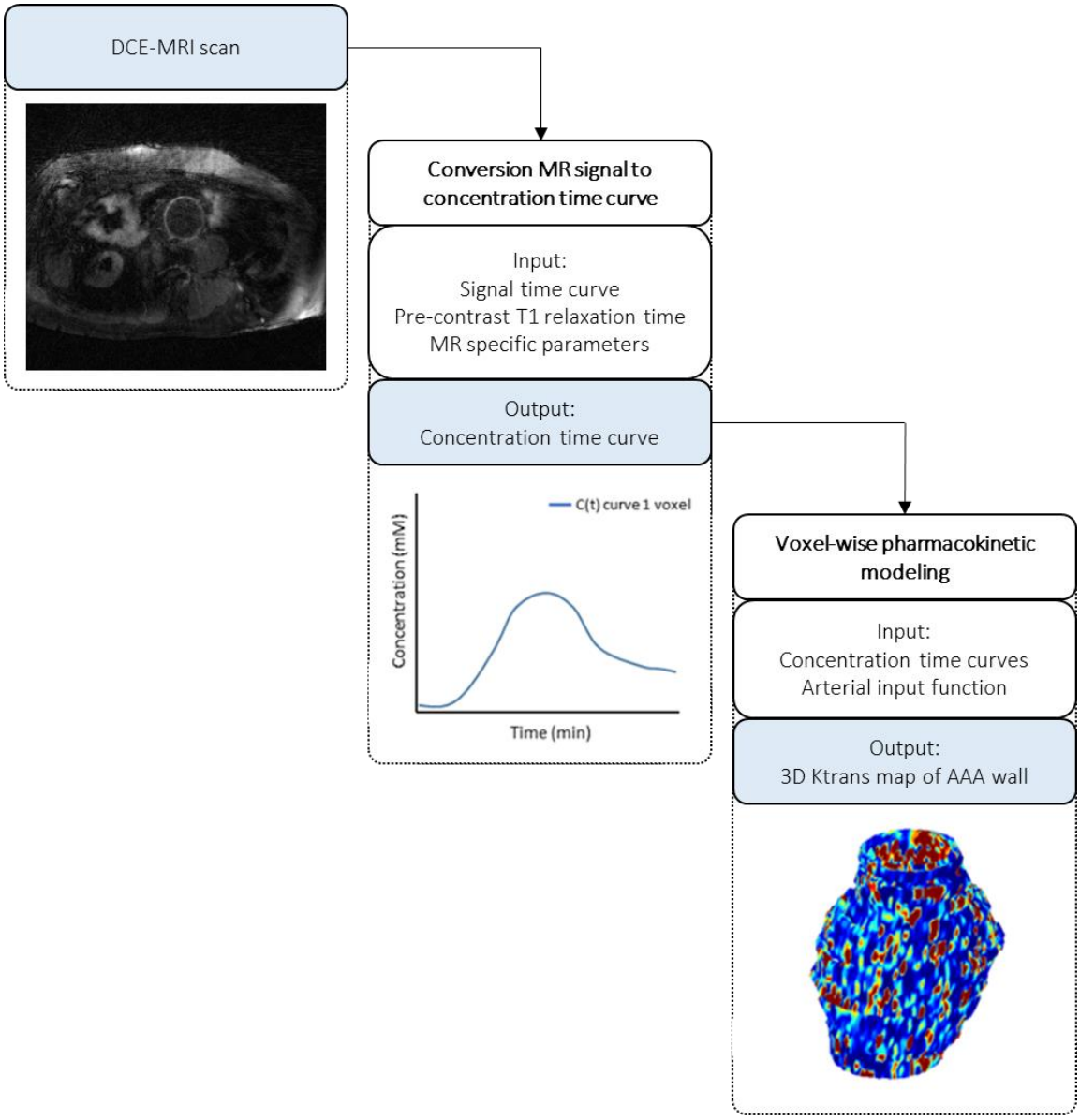

Figure 4. A flowchart of the steps to generate K_{trans} parameter maps by analyzing Dynamic Contrast Enhanced MRI scans.

2.2.3 Acquisition DCE-MRI scans

To obtain images with the desired image contrast, multiple MRI sequences with a different number of radiofrequency pulses and gradients can be used. DCE-MRI scans are usually performed with a T1-weighted imaging sequence and 2D or 3D dynamic acquisition such as a Fast Field Echo (FFE) sequence. (32) The signal of this FFE sequence is described by:

$$S(t) = M_0 \frac{1-E_1}{1-E_1 cos\alpha} . \sin(\alpha) \quad [1]$$

where M_0 is the net magnetization signal before contrast arrival, α is the flip angle, and E_1 represents the longitudinal (T1) relaxation and is described by:

$$E_1 = e^{-TR/T_1(t)} \quad [2]$$

with the sequence's repetition time (TR) and $T_1(t)$ relaxation time over time of contrast injection. M_0 can be calculated using the pre-contrast T1 (T10) relaxation time and Eq. [1] of the signal $S(t)$ before contrast arrival. (33)

However, in DCE-MRI acquisition for AAAs, there are two competing requirements. First, a high temporal resolution bright-blood imaging is required for measurement of the input of contrast. Second, a high spatial resolution black-blood imaging is required to distinguish the AAA wall from the lumen (34).

To allow assessment of AAA wall perfusion, a 3D black-blood Turbo Field Echo (TFE) DCE-MRI sequence can be used. This sequence suppresses blood signal by an improved motion-sensitized driven-equilibrium (iMSDE) pre-pulse to distinguish the vessel wall. However, the input of contrast cannot be measured because of the black blood contrast, nonetheless, there are alternative methods to obtain the concentration time curve of the CA. (34) The signal of the 3D black blood TFE sequence is described by:

$$\mathrm{S(t)} = M_0 \frac{(1-E_1)E_2 sin\alpha}{1-E_1 cos\alpha} \cdot \frac{1-(E_1 \cos(\alpha))^K}{1-E_2(E_1 \cos(\alpha))^K} \quad [3]$$

where K is the shot length, and E_2 represents the transverse (T2) relaxation which is described by:

$$E_2 = e^{-T_{2\,\mathrm{prep}}/T_2(t)} \quad [4]$$

with $T_2(t)$ relaxation time over time of contrast injection and $T_{2\,prep}$ is the duration of the iMSDE pulse (34). M_0 in Eq. [3] can be calculated using the tissue's T10 and pre-contrast T2 (T20) relaxation times and Eq. [3] of the signal $S(t)$ before contrast arrival. To calculate the signal before contrast arrival the frames before contrast injection are used, the so-called baseline scans. (33)

Additionally, the tissue-specific relaxation times T10 and T20 are required for conversion of the signal into a concentration time curve. T10 and T20 of all individual voxels can be estimated by T1- and T2-mapping. A commonly used technique for T1-mapping is to scan with varying flip angles and for T2-mapping scanning with varying echo times is performed. Subsequently, equations describing the signal intensity, such as Eq. [1] or [3] to calculate the tissue-specific pre-contrast relaxation times, can be used to obtain tissue-specific T1 and T2 times. Mapping the pre-contrast relaxation times allows for individual relaxation times per voxel. Alternatively, T1 and T2 relaxation times of the tissue of interest from literature can be used whereby the relaxation times are similar for all voxels. (30, 35)

2.2.4 Conversion MR signal to concentration time curves

Conversion of the signal to concentration time curves is one of the most important factors affecting the estimation of physiological parameters of the AAA wall. The concentration time course can be obtained by correlating the dynamic changes in signal intensity with the tissue-specific T10 time. Moreover, the relationship between signal and contrast concentration depends on MRI parameters such as T10, flip angle, TR, and relaxivity of the contrast agent (33, 36).

The concentration can be estimated for a T1-weighted sequence using the following equation:

$$C(t) = \frac{1}{r_1}\left(\frac{1}{T_1(t)} - \frac{1}{T_{10}}\right) \quad [5]$$

where r_1 is the relaxivity of the contrast agent. T_{10}, can be obtained via T1-mapping or a value from literature can be used. $T_1(t)$ can be derived by solving Eq. [1] using Eq. [2] for $T_1(t)$. (33)

When another sequence is used in which a T2 relaxation pulse is given, such as the 3D black-blood TFE sequence, the T2 relaxation times should also be taken into account when converting the signal time curves to concentration time curves (34). In this case, to calculate $C(t)$, Eq. [3] can be solved for $T_1(t)$ and $T_2(t)$ using Eq. [2] and [4].

2.2.5 Arterial input function

In addition to the concentration curves of the AAA wall, the concentration time curve of the contrast in blood plasma must be calculated. The concentration time curve of the contrast in the blood plasma is called the arterial input function (AIF).

Measurement of the AIF from DCE-MRI images of the AAA wall is challenging because of the high temporal resolution (<1s) per frame that is required. Moreover, another requirement for measurement of the AIF is bright-blood contrast which cannot be fulfilled in DCE imaging of the AAA wall. (6) An alternative way to measure the AIF is invasive via blood sampling during image acquisition. A more simplistic way to obtain the AIF is using a population-based AIF that assumes a fixed AIF. (29, 30)

Parker et al. (37) have developed a model for the AIF of the aorta. They have estimated an average AIF of 67 patients. This population-based AIF shows the peak of the first contrast pass, a recirculation peak and a prolonged washout as shown in Figure 5. By modeling this AIF into a function, the AIF can be used as input in low temporal resolution and black blood DCE-MRI acquisitions. (37, 38)

A gadolinium-based contrast agent is distributed in plasma rather than whole blood. Therefore, effective plasma concentrations should be considered. The ratio of plasma to whole blood depends on the hematocrit, which is the percentage of red blood cells in the blood and is usually 40%. (28)

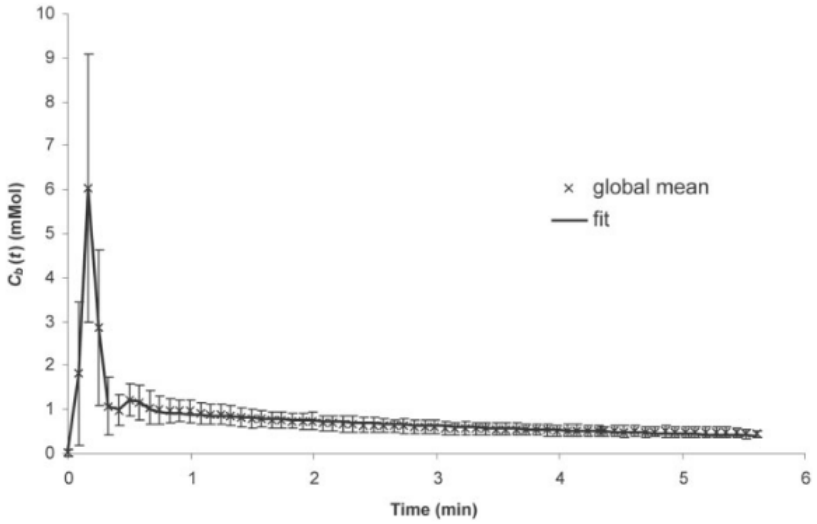

Figure 5. Fit (line) and global means (crosses) of the high temporal resolution population-based arterial input function of the aorta from Parker et al. (37) Error bars depict ±1 standard deviation across the population of 67 AIFs.

2.2.6 Pharmacokinetic modeling of the AAA wall

The final step in obtaining parameter maps is to perform physiological-based analysis through mathematical PK models. Several PK models can be used to cope with the DCE-MRI acquisition challenges for the aortic wall.

The most commonly used model is the extended Tofts (ETofts) model which assumes bidirectional exchange of contrast between the blood plasma volume and EES. The Patlak model is more simplistic since it assumes there is no efflux from EES to the blood plasma volume. (30, 39) Figure 6 visualizes the ETofts model and Patlak model. Both models require an AIF as input. However, a population-based AIF also suffices so scanning with high temporal resolution or bright-blood sequence is not essential.

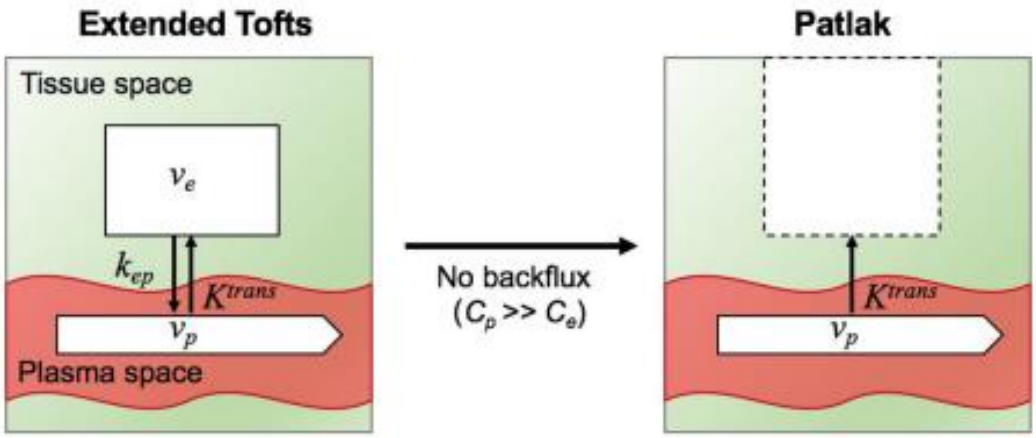

Figure 6. Extended Toft model (left): a two-compartment model that considers the blood plasma to be the central compartment (v_p), and the extravascular-extracellular space (EES) to be the peripheral compartment (v_e). In this model, the contrast agent is introduced into the vasculature and transported into the EES in a reversible process characterized by a distribution rate constant (K_{trans}) and a redistribution rate constant (k_{ep}). Patlak model (right): this model only considers the perfusion of contrast out the vasculature system into v_e and ignores the back flux into v_p. (40)

The ETofts model describes the contrast agent concentration in the tissue by:

$$C_t(t) = v_p\, C_p(t) + K^{trans} \int_0^t C_p(\tau)\, e^{-(\frac{K_{trans}}{v_e})(t-\tau)} d\tau \,. \qquad [6]$$

By fitting the concentration time curve of each voxel to the ETofts model as in Eq. [6] using the AIF ($C_p(t)$) as input, physiological parameter maps of K_{trans}, v_e, v_p, and k_{ep} which is described by K_{trans}/v_e, can be calculated. t is the time point at which the amount of contrast in the tissue is measured. (28)

In addition to the ETofts and Patlak model, other PK models are developed to overcome technical challenges of scanning with a black-blood sequence and still obtain the AIF for each patient individually. Ahmed et. al (4) developed a constrained extended reference region model (CERRM). This type of PK model bypasses the direct AIF measurement but instead uses relative contrast concentrations in a reference region such as muscle. As a result, scans can be performed with a high spatial resolution and black-blood contrast. (4, 41)

Researchers in the Amsterdam UMC have improved the CERRM from Ahmed et al. (4) by the addition of constraints and quantified K_{trans}. Signal evaluation showed sufficient suppression of the blood signal. A feasibility analysis including six patients indicated that the CERRM-based AAA K_{trans} calculations were moderately reproducible with a coefficient of variation (CoV) of 49%.

2.2.7 Fitting pharmacokinetic models

To obtain the DCE-MRI parameter maps, a fitting of the preferred PK model to the concentration curves can be performed.

2.2.7.1 Least Squares fitting method

A conventional way to fit the ETofts model is to perform a voxel-wise nonlinear least squares (LSQ) fitting. During LSQ fitting the values of the fitting parameters, v_e, v_p, k_{ep}, K_{trans}, dt (time of contrast arrival) in Eq. [6] are varied to find the optimal parameter combination that best fits the concentration curve of the voxel. (29) However, the acquired concentration time curves are generally noisy, hence the LSQ fitting may yield parameter estimates with large variance and bias. Moreover, the fitting may converge to a suboptimal solution because the LSQ objective can have multiple local minima. As a result, LSQ fitting of DCE parameters may have poor reproducibility. (40, 42)

2.2.7.2 Deep learning methods

Recently, artificial intelligence techniques such as deep learning networks have been investigated for the application in medical image analysis for tasks such as parameter estimation. A neural network can search for the optimal parameter combination and reconstruct the original curve through the defined PK model. (42, 43)

A deep learning network may outperform the LSQ fitting because such a network can generalize well over large datasets, and besides, they are computationally faster. Therefore, it may be more robust to noisy voxels and have a lower signal-to-noise ratio as compared to a conventional LSQ fitting. However, the generalization could also be a disadvantage since it could result in bias. (40, 42)

For parameter estimation in DCE-MRI, recurrent neural networks may be suitable since they can handle varying data acquisition lengths. Especially Long Short-Term Memory (LSTM) (44) networks and Gated Recurrent Units (GRUs) (45) have been successfully applied to learn temporal relationships in sequential data. GRUs comprise fewer parameters but exhibit similar performance as LSTM networks and therefore GRUs may perform better on smaller datasets. (42, 43, 45)

Ottens et al. (42) developed a deep learning DCE-MRI parameter estimation network (DCE-net). The DCE-net utilizes GRUs combined with attention layers and learns to estimate the physiological parameter from the DCE-MRI concentration time curves. The network learns to fit the concentration curves to the ETofts model using unsupervised learning approaches since ground truth parameters cannot easily be obtained from in vivo data. The unsupervised learning is based on a physics-informed loss function which is the mean squared error between the estimated and measured concentration curves. (42)

3 Aim of the thesis

In the Amsterdam University Medical Centers (UMC), novel biomarkers for AAA progression and rupture are being researched to complement the currently used aortic diameter. The quantification of K_{trans} in AAAs in three dimensions is studied. Fast volumetric black-blood DCE-MRI sequences were in-house developed and multiple patients had been scanned twice with this protocol.

The aim of this thesis is to investigate K_{trans}, a novel potential biomarker for AAA progression, risk of rupture and clinical benefit.

DCE-MRI is a relatively new technique and has, to the best of our knowledge, never been performed in 3D for the AAA wall. Therefore, methods needed to be improved and tested for this application. This thesis consists of two parts that will be addressed to give insight into the potential biomarker K_{trans} for the application in AAAs.

First, DCE-MRI data will be analyzed to quantify the potential biomarker K_{trans}. Two methods to calculate K_{trans} will be evaluated for the application in the AAA wall. The first method uses an LSQ fitting of the PK model and the second method uses a deep learning network to estimate the parameter maps of K_{trans} with the use of the same PK model. To assess the reliability of the methods, scan and rescan reproducibility of the K_{trans} calculations will be calculated for both methods.

Second, the use of the biomarker K_{trans} in clinical practice will be evaluated. The clinical interpretation of K_{trans} as a biomarker can be assessed by associating calculated values of K_{trans} of the AAA wall with disease progression and AAA diameter.

This master thesis is in line with the objectives of the MARVY project; the development of *MRI-based endovasculAR procedures for Vascular surgerY*, which recently started in the Amsterdam UMC. MARVY aims to convert vascular surgery practice by introducing MRI-based clinical decision-making and endovascular therapy. The results of this thesis can be used to evaluate whether changes in the DCE protocol are be made before scanning new patients within the MARVY project.

4 Materials and Methods

4.1 Patients

Patients with an asymptomatic infrarenal AAA of at least 30 mm diameter were included in the clinical study titled 'Advanced MRI in AAA' performed in the Amsterdam UMC between 2017-2019. This study was conducted in accordance with the Declaration of Helsinki, the approval of the ethics committee of the Academic Medical Center and all patients gave written informed consent.

Exclusion criteria were supra- or pararenal AAAs, previous AAA repair, contra-indications for MRI (e.g. presence of a neural stimulator, drug pump or history of working with metal), reduced renal function (eGFR <30), previous allergic reactions to intravenous contrast agents, an inflammatory, infectious or mycotic AAA, vasculitis and connective tissue disease.

Patients were included for the Advanced MRI analysis in AAA study (n=26). One participant did not want to proceed scanning during the start of the first scan. Due to technical issues in five patients both DCE-MRI scans failed and in three patients one scan failed. As a result, seventeen patients underwent two consecutive scans at a one-week interval and three patients had one scan, resulting in a total of 37 DCE-MRI scans. In this thesis, the first DCE-MRI scan was referred to as 'scan' and the second DCE-MRI scan was referred 'rescan'.

4.2 Study design

This study was a single-center cross-sectional cohort pilot study to assess reproducibility and clinical value of K_{trans} calculations of prospectively collected 3D DCE-MRI data of the AAA wall. The primary end point of this thesis was the reproducibility of two methods, the LSQ fitting and DCE-net, which calculate K_{trans} on DCE-MRI images. The secondary end point was the clinical value of K_{trans} as a biomarker for AAA progression and rupture. To give insight into the reproducibility and clinical value of K_{trans}, the steps visualized in Figure 7 were executed.

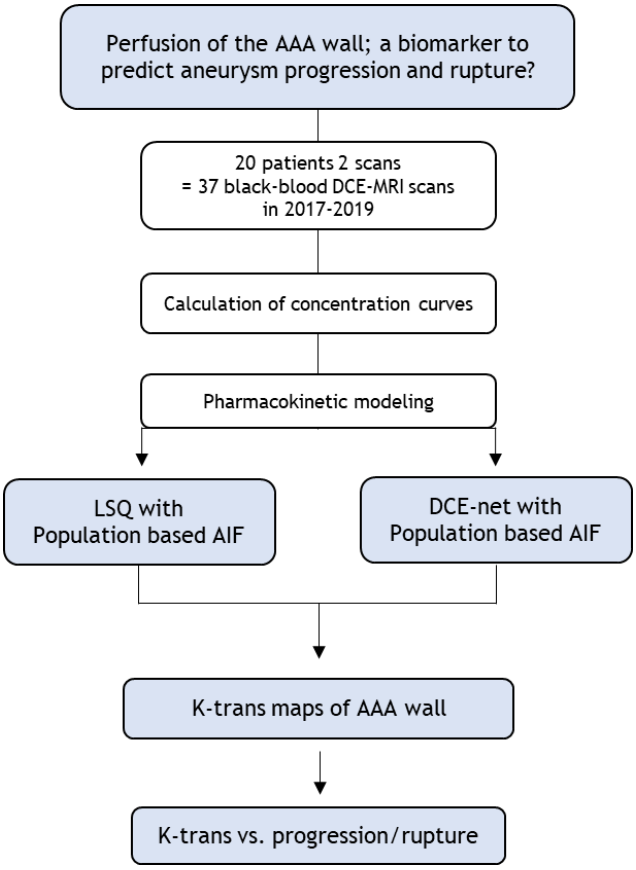

Figure 7. A flow chart of the study design of the thesis. AAA = Abdominal Aortic Aneurysm, DCE-MRI = Dynamic Contrast Enhanced MRI, LSQ = Least squared, AIF = Arterial Input Function, DCE-net = deep learning DCE-MRI parameter estimation network

4.3 Data

4.3.1 Acquisition DCE-MRI scans

Scans were performed with a 3D black-blood TFE DCE-MRI sequence that was developed for this study. The blood signal was suppressed by an iMSDE pre-pulse and a CHESS fat-suppression pre-pulse was given at the beginning of each TFE shot. The fat suppression pulse caused additional T1 relaxation and the black blood pulses resulted in additional T2 relaxation.

All scans were performed on the Philips Ingenia 3T MRI system. Scanning was performed before and after intravenously injection of the contrast agent Gadobutrol (Gadovist; 0.1 mmol/kg). The scans had a voxel size of 1.2x1.2x3 mm and a field of view of 420x420x87 voxels. Each scan consisted of 29 slices and each slice had 46 timeframes visualizing the uptake of the contrast agent. The temporal resolution was 8.5 seconds per frame resulting in a total scanning time of 6.5 minutes.

The DCE-MRI scans were able to capture signal enhancement over time as a result of contrast uptake in the AAA wall (Figure 8). The signal enhancement of one voxel is represented by a signal time curve (Figure 9).

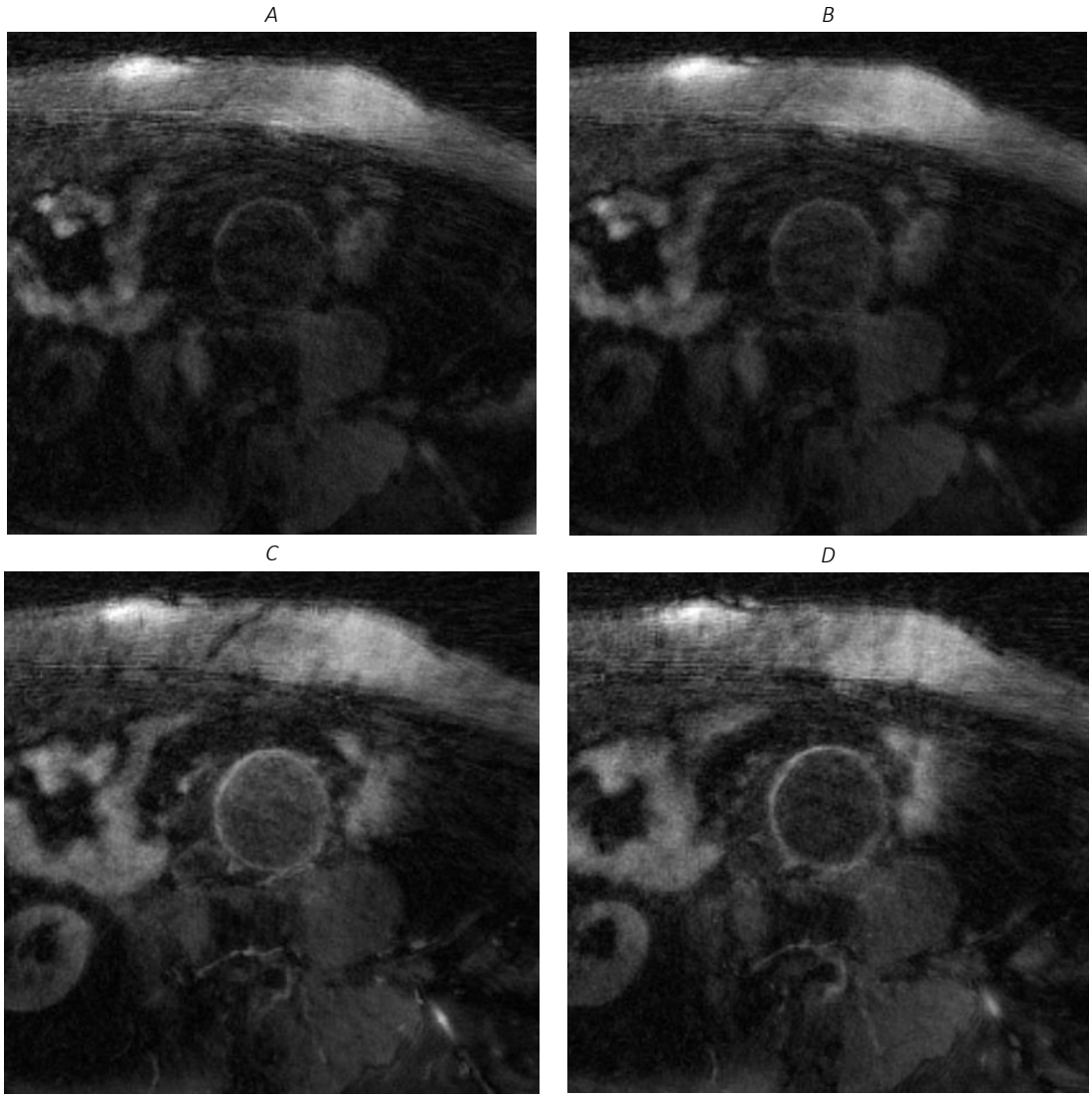

Figure 8. Example figure of contrast enhancement for four timeframes of one axial slice of a Dynamic Contrast Enhanced (DCE) MRI scan from the study. One DCE-MRI scan consists of 46 timeframes, of which frame (A); precontrast, (B); arrival of contrast, 15 (C); peak of contrast in AAA wall, and contrast removal (D) are visualized.

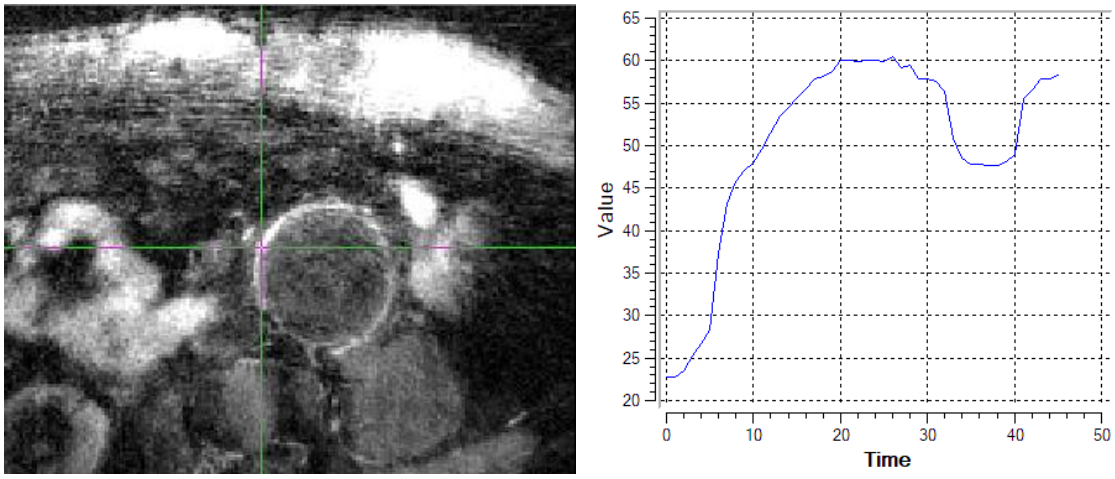

Figure 9. A selected voxel in the AAA wall is marked by the intersection of the green/pink lines (left) and the signal time curve of the selected voxel (right). A signal increase can be seen when the contrast agent arrives starting at timeframe 5.

4.3.2 Annotation of the aneurysm wall

The region of interest (ROI) was the AAA wall which was annotated slice-by-slice by a Technical Physician in the Amsterdam UMC using dedicated post-processing software Vesselmass (Leiden University Medical Center, the Netherlands). The wall was annotated to create 3D labels of the vessel wall of all DCE-MRI scans as in Figure 10. The 3D labels were used to select the signal time curves of the aneurysm wall. The wall was annotated on consecutive slices on which the contours of the AAA wall can be distinguished. As a result, annotations consisted of 15 to 29 slices. To inspect the amount of signal enhancement in the annotated AAA wall masks, the signal enhancement of background voxels and the AAA wall mask was visualized.

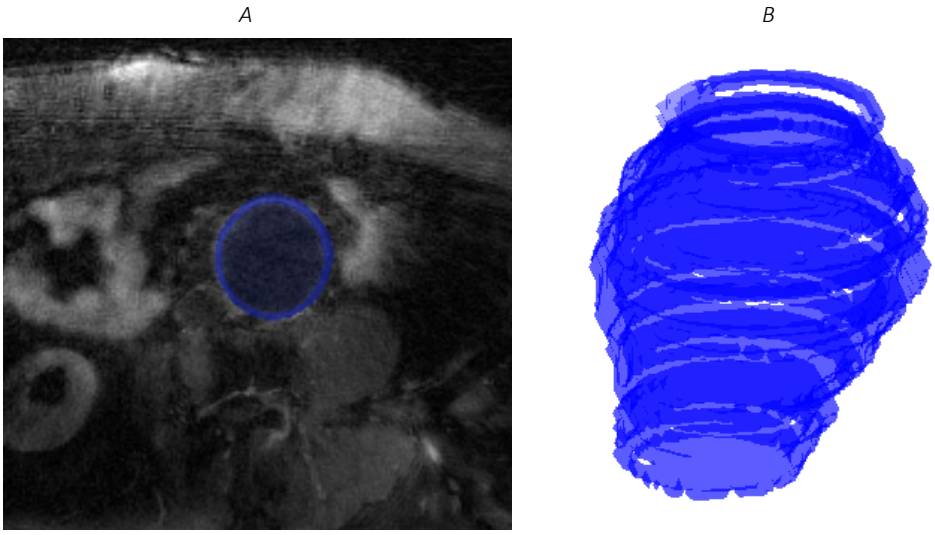

Figure 10. (A) An axial slice of a Dynamic Contrast Enhanced MRI scan including the annotated mask of the region of interest; the AAA wall, in blue. (B) The annotated AAA wall mask in 3D.

4.4 Calculation of K_{trans} maps

For the calculation of K_{trans} parameter maps multiple steps needed to be executed. First, the signal intensity time curves were converted into concentration time curves using the tissue-specific T10 and T20 values and MRI specific parameters. Subsequently, to obtain physiological parameter maps, the concentration time curves were fitted to the Etofts PK model with use of the AIF. Two fitting techniques, the LSQ fitting and a deep learning approach, were used. (29)

4.4.1 Conversion MR signal to concentration time curves

4.4.1.1 Previously generated concentration time curves

The concentration time curves of all patients were already generated by former researchers in the Amsterdam UMC. The DCE-MR signal for the used TFE sequence with black blood and fat suppression pre-pulses had both T1 and T2 weighting. (34) Therefore, the DCE signal intensity time curves were converted to concentration curves by a voxel-wise nonlinear fit of the signal described by Eq. [3]. Appendix A1 describes the MRI parameters that were used for the conversion of the signal to concentration. Concentration time curves of voxels in the AAA wall were generated by using signal Eq. [3] and scan specific MRI parameters. To give an example of these curves, 100 random concentration curves of the AAA wall of one patient were visualized in Figure 11.

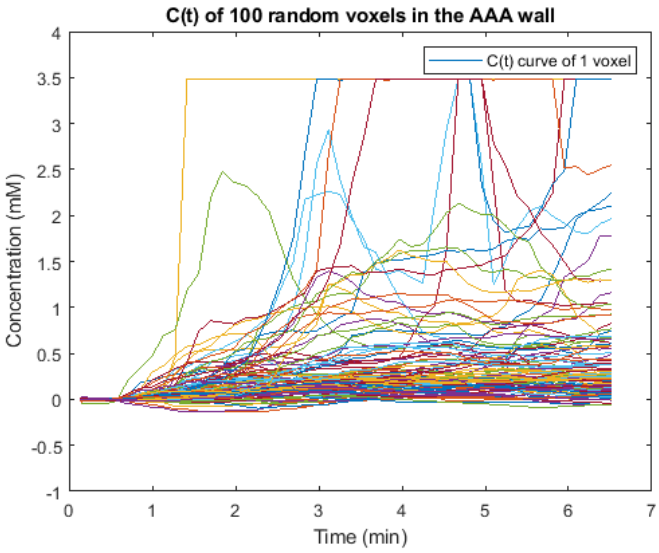

Figure 11. Concentration time curves (C(t)) calculated from signal intensity curves with Eq. [3] of one patient of 100 random voxels in the Abdominal Aorta Aneurysm wall. The curves have a maximum concentration value of 3.5mM.

4.4.1.2 Generation of new concentration time curves

The concentration curves of the AAA patients visualized in Figure 11, calculated with Eq. [3], showed an abnormal threshold at the concentration value of 3.5 mM. Such a threshold results in abnormal concentration curves, making further analyses unreliable and unrealistic. Therefore, the origin of this behavior was investigated and a solution to omit such curves was searched. To give insight into the origin of the threshold of the concentration time curves, the signal was simulated for multiple contrast concentrations.

After simulation (see results) of the signal against different contrast concentrations it became clear that the conversion of signal to concentration using Eq. [3] caused this behavior, and hence, worked poorly for our DCE dataset. New concentration curves were calculated for further analyses with a simplistic equation for the signal such as Eq. [1]. This equation describes the MR signal for a standard DCE-MRI sequence that ignores the effect of the fat-suppression and black blood pulses.

Inputs for Eq. [1] are the signal intensity time curves, T10 of the AAA wall, MR parameters, and the relaxivity of the contrast agent (33). The signal intensity time curves were calculated only for the AAA wall by application of the annotated mask of the AAA wall. The concentration curves were calculated only for the voxels in the AAA wall since this is the region of interest and computation time will be minimized by leaving out other voxels. The required MR parameters are described in Appendix A2. The scan-specific inputs were derived from DICOM tags and T1 relaxivity of the contrast agent Gadovist was defined as 5 mM (46). T10 was set to 1.150 s as described by Qi et al. (34). After evaluation of the contrast arrival, the number of baseline scans, which was needed to calculate the baseline MR signal, was set at five frames.

Subsequently, the reliability of the newly generated concentration time curves was evaluated by analyzing the corresponding signals. Following this analysis, post-processing steps needed to be performed to obtain realistic concentration curves.

4.4.2 Arterial input function

In addition to the concentration curves of each voxel, the AIF must be defined before PK modeling can be performed. The temporal resolution of the DCE-MRI scans to image one timeframe of the 3D AAA wall was 8.5 s, which was too high to measure the AIF. More importantly, the AIF cannot be determined because of the black-blood sequence used to create the DCE-MRI images. (32) Therefore, the population-based AIF from Parker et al. (37) was used. The AIF was corrected for hematocrit in the blood to obtain effective plasma concentrations. Furthermore, the first time point (t0) of the AIF was set to zero. Figure 12 visualizes the used AIF from Parker et al. (37) in blue and in orange the AIF that was corrected for hematocrit and t0.

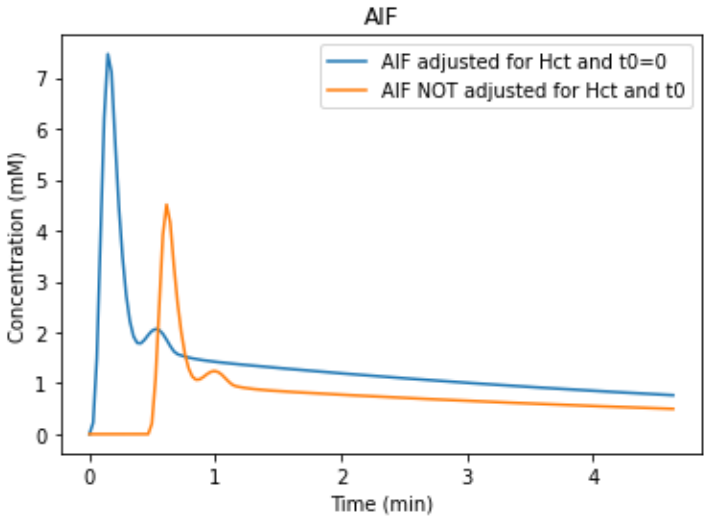

Figure 12. Arterial Input Function (AIF) of the aorta from Parker et al. (37) in blue. In orange, the AIF corrected for hematocrit (Hct) in the blood and correction of the time of arrival of the contrast (t0).

4.4.3 Fitting pharmacokinetic models

In this thesis, two different methods to fit the concentration curves to the ETofts model were analyzed (LSQ fitting and DCE-net). Both fitting methods computed the same output which were the parameter maps of v_e, v_p, k_{ep}, dt, and K_{trans}. The LSQ fitting of the ETofts model (Eq. [6]) will be used for comparison with the new DCE-net fitting method. The DCE-net is a fitting method of the ETofts model the department of radiology in the Amsterdam UMC is currently working on. (42) The CERRM method that was investigated by researchers in the Amsterdam UMC a few years ago was not assessed in more detail.

4.4.3.1 Least Squares fitting

The voxel-wise LSQ fitting of the ETofts model was performed on the concentration curves of the AAA wall for each patient using the corrected AIF in Figure 12 in Python version 3.9.7. To minimize the infinitely many possible values of the fitting parameters, boundary conditions were defined. Also, initial values were given as a starting point for the fit. Lower boundaries for [k_{ep}, $dt(\mathrm{min})$, v_e, v_p] were set to [0.0, 0, 0.0, 0.0] and upper boundaries were [5.0, 2, 1.0, 1.0], initial values were [0.6, 1, 0.03, 0.0025].

After fitting the concentration curves k_{ep}, dt, v_e, v_p were calculated for each voxel. By combining all voxels of the AAA wall, 3D parameter maps were generated. A parameter map of K_{trans} was calculated by $k_{ep} * v_e$.

4.4.3.2 DCE-net

The DCE-net of Ottens et al. (42) was trained in Python version 3.9.7 and Pytorch version 1.10.2. The concentration curves of each voxel were given as input and the DCE-net was trained to return the fitting parameter maps of v_e, v_p, k_{ep}, dt, K_{trans}. Data used for training and validation was one large dataset with generated AAA wall concentration curves of 37 available DCE-MRI scans. The dataset consisted of 220.000 concentration curves of AAA wall voxels of which 90% (200.000) was used for training and 10% (20.000) for validation. Also, the corrected AIF in Figure 12 was given as input for the network.

During training, different sizes of batch sizes and learning rates were explored. Finally, the network was trained with a batch size of 128 using an Adam optimizer. A learning rate of $0.5e^{-3}$ was used with a patience of 3. The learning rate was reduced by 0.1 when the network did not improve within 3 epochs. Training was performed in 35 epochs which took 1 hour.

The DCE-net learned via a physics-informed unsupervised approach since there was no ground truth. The performance of the network was assessed based on the loss function. The loss is calculated by the mean of the mean squared error between the estimated concentration curves and the original concentration curves of all voxels.

Subsequently, for each patient separately, the concentration curves of the AAA wall were given as input to trained DCE-net to generate the parameter maps. Consequently, parameter maps of k_{ep}, dt, v_e, v_p and K_{trans} were calculated for each patient.

4.5 Reproducibility analysis K_{trans} maps

A quantitative assessment was performed by comparing scan and rescan reproducibility of the K_{trans} maps generated with both the LQS fitting and the DCE-net. Before generating reproducibility plots, the effect of minor changes in position and movement of the patient between scan and rescan was minimized by pre-processing steps.

To enable a fair comparison between the K_{trans} maps of scan and rescan, the two scans need to be aligned. Therefore, registration of scan and rescan was performed in Matlab version 2021b (Mathworks, USA). Built-in functions for intensity-based registration for translation transforms were used to avoid unrealistic shapes of the AAA wall. The registration was performed on NIfTI images that are averages of all timeframes of the scans and applied to the 3D K_{trans} maps. Figure 13 displays an example of a registration of scan and rescan. After the registration, the overlapping slices of scan and rescan can be compared.

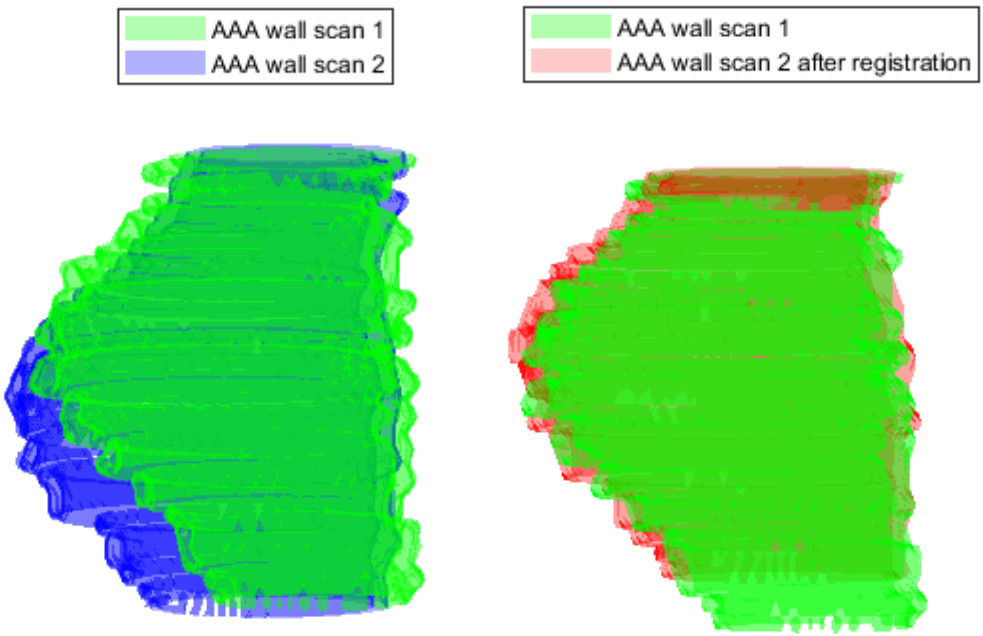

Figure 13. Visualization of the annotated AAA wall of the first (green) and second (blue) scan before registration (left) and after registration (right) of the second scan (red) to the first scan (green).

Voxel-wise comparison of the registered K_{trans} maps may still be too sensitive for errors since patients were scanned at a one-week interval. Therefore, the reproducibility was assessed by comparison of larger areas of scan and rescan.

First, the AAA wall was divided into small segments to assess the reproducibility between scan and rescan of the two methods to quantify K_{trans}. The K_{trans} maps were divided into pie-shaped segments with a size of 1-2cm (Figure 14). The mean K_{trans} of these small segments can be compared for scan and rescan. To obtain segments with a size of 1-2cm, the 3D volume of the AAA wall was divided into eleven quadrants in the x- and y-direction based on centroid and into five equal segments in the z-direction for all patients. As a result, pie slice shaped segments were generated and K_{trans} means were calculated of these segments. Segments had a size of 1-2 x 1-2 x 1-1.7 cm which consisted of around 50-100 voxels. The variation in size of the segments was caused by the circumference and length differences of the annotated AAA labels.

Second, larger segments were compared between scan and rescan to assess the reproducibility of the two fitting methods (Figure 15). These large areas may be clinically more interesting since the small segments may consist of too much detailed information for clinical use. The mean K_{trans} value of large areas may indicate weakened regions of the AAA wall to indicate where it could rupture. The aneurysm was divided into the larger segments using the same method as was used for the small segments. The 3D K_{trans} maps of the AAA wall were divided into four quadrants in the x- and y-direction based on centroid and into two equal segments in the z-direction for all patients. As a result, pie slice shaped segments were generated and K_{trans} means were calculated of these segments with a size of around 3-4.5 x 3-4.5 x 2.5-4 cm.

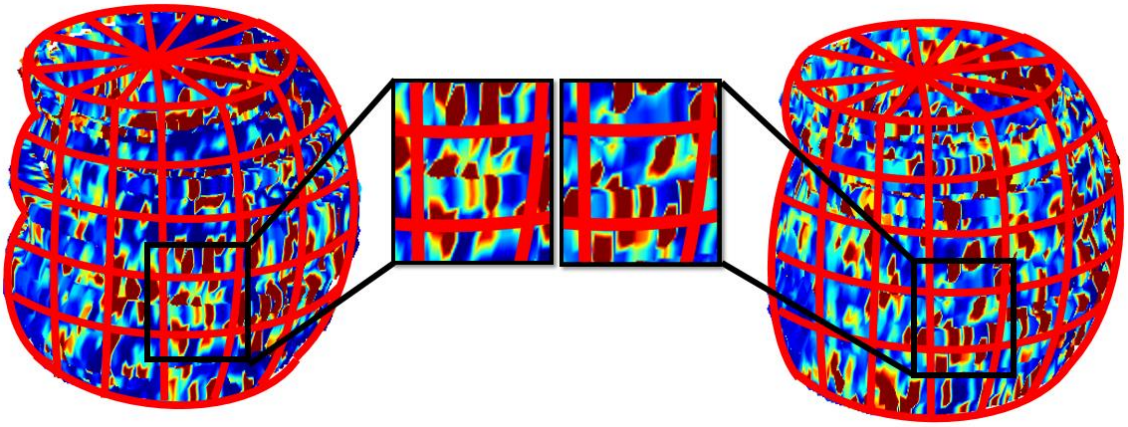

Figure 14. A schematic example of the small segments (1-2 cm) of the K_{trans} maps that were compared for the first (right) and second (left) scan. The magnified squares illustrate the segments of which the median K_{trans} values were compared .

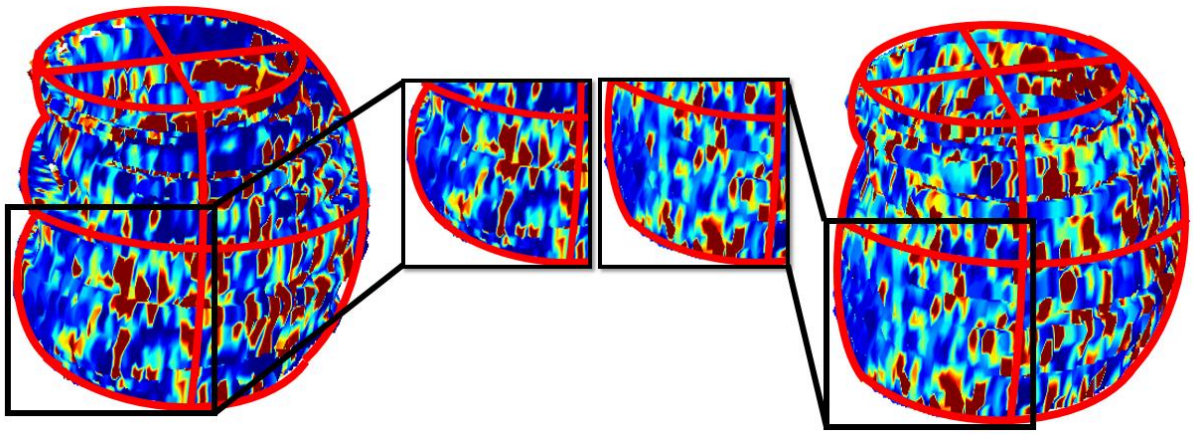

Figure 15. A schematic example of the large segments (3-4 cm) of the K_{trans} maps that were compared for the first (right) and second (left) scan. The magnified squares illustrate the segments of which the median K_{trans} values are compared.

At last, scan-rescan reproducibility of median and maximum K_{trans} values was assessed for the fitting method that seemed most reproducible. The median K_{trans} value of the whole annotated AAA and the median K_{trans} value of the slices with maximal diameter were calculated and assessed for can-rescan reproducibility. Also, the maximum K_{trans} values were evaluated for scan and rescan. The reproducibility of the 95th percentile K_{trans} value of the whole annotated AAA and 95th percentile K_{trans} value of the slice with maximal AAA diameter was calculated. Medians instead of means, and 95th percentiles instead of maximums were quantified to minimize the effect of outliers.

4.6 Clinical analysis K_{trans} maps

Since the aortic diameter is currently the golden standard for clinical decision making, K_{trans} of the AAA wall was compared with AAA diameter. To assess the relation between K_{trans} and progression of the AAA, the parameter maps were compared to aneurysm growth.

The patient files of all patients that underwent DCE-MRI scans were analyzed for disease progression. Two patients had no available surveillance imaging and could not be used for clinical analysis. Therefore, the clinical analysis was performed on eighteen patients. in three of these patients only one DCE-MRI scan was performed successfully. Consequently, K_{trans} maps of sixteen first DCE-MRI scans and seventeen second DCE-MRI scans were compared to clinical data.

For all patients, aneurysm growth was obtained via available follow-up imaging which was ultrasound in most cases. Maximal AAA diameters in the anterior-posterior (AP) direction were acquired from notes of ultrasound follow-up imaging from 2013-2022. Subsequently, the aneurysm growth per year was calculated from which the mean and maximum growth during available follow-up could be determined for each patient. Also, the cause of death was obtained for patients that died during follow-up. The maximal diameters of the annotated AAA wall were calculated automatically using Matlab.

The K_{trans} maps generated with the method that seemed most reproducible were used for the clinical analysis. To compare the volumetric parameter maps of K_{trans} to aneurysm diameter and growth, the maps were compacted into one K_{trans} value. K_{trans} values of the whole annotated AAA, the median K_{trans} values of the slices with maximal diameter, the 95th percentile K_{trans} values of the whole annotated AAA and the 95th percentile K_{trans} values of the slice with maximal AAA diameter were compared to diameter and AAA growth.

4.7 Statistical analysis

4.7.1 Reproducibility analysis K_{trans} maps

Reproducibility was assessed by a correlation plot and Bland-Altman plot with coefficient of variation (CoV). CoV represents the extent of variability in relation to the overall mean of K_{trans} for the two consecutive scans and is defined by

$$CoV = \frac{Standard\ deviation}{Mean\ of\ population}. \quad [7]$$

Correlation and Bland-Alman plots were created in which the K_{trans} values of scan and rescan were compared using Matlab. The difference of K_{trans} in the Bland-Altman plot was calculated by subtracting the first scan from the second scan.

First, plots were generated for both LSQ and DCE-net fitting methods for the small K_{trans} segments. In one plot for one method, data of all seventeen patients were combined. Plots were generated for each patient individually to evaluate interpatient variability. Besides, the mean value of the difference between the first and second was tested for statistical significance using IBM SPSS Statistics for Windows, Version 26.0. To evaluate whether the mean value of the difference differed significantly from 0, a one-sample t-test was used. In case the p-value is <0.05, the mean value of the difference is significantly different from 0, meaning there is a fixed bias between scan and rescan.

The same plots as for the small K_{trans} segments were generated for the larger segments in which the mean K_{trans} values of scan and rescan were compared. For the LSQ method, the reproducibility of median, and maximal K_{trans} values of scan and rescan was assessed by correlation and Bland-Altman plots.

4.7.2 Clinical analysis K_{trans} maps

Pearson correlations between K_{trans} values generated using the LSQ fitting method and AAA diameter and progression were calculated. The following parameters were analyzed: the median K_{trans} values of the whole annotated AAA, the median K_{trans} values of the slices with maximal diameter, the 95th percentile K_{trans} values of the whole annotated AAA and the 95th percentile K_{trans} values of the slice with maximal AAA diameter. These K_{trans} parameters were compared with the diameter measured using ultrasound and with the mean progression per year and maximum progression in one year. In case the Pearson correlation was significant, correlation plots were generated.

5 Results

5.1 Patients

Baseline characteristics of the 20 included patients are described in Table 1.

Table 1. Baseline characteristics of patients included in the study Advanced MRI in AAA. Numbers are presented as n (%), mean ± standard deviation. COPD = chronic obstructive pulmonary disease.

	# patients (*n* = 20)
Males	18 (90%)
Age at time of scan	71 (66-76)
Cardiovascular comorbidity	12 (60%)
Hypertension	11 (55%)
COPD	5 (25%)
Diabetes mellitus	3 (15%)
Smoking	
Current smoker	5 (25%)
Not a smoker	5 (25%)
Stopped	10 (50%)

5.2 Signal enhancement AAA wall masks

The amount of signal enhancement of the DCE-MRI images visualized for three patients (Figure 16). The yellow voxels depict the overlay between the AAA wall mask (green) that have a high signal enhancement (blue).

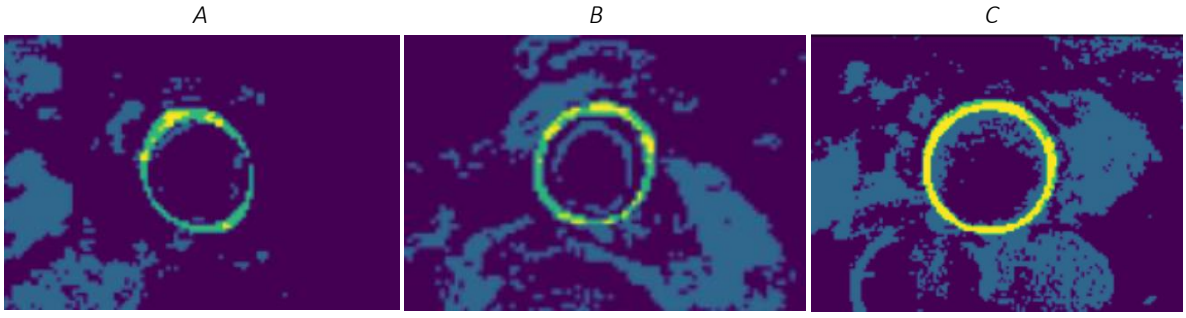

Figure 16. Visualization image of signal enhancement by contrast injection of three DCE-MRI scans (A,B,C). Voxels with a high enhancement in blue, in green the annotated AAA wall, in yellow the overlap between the blue and green, and in purple background voxels with little signal enhancement. Scan A, B have little enhancement in the AAA wall whereas scan C has a high signal enhancement in the AAA wall.

5.3 Conversion MR signal to concentration time curves

To understand the origin of the threshold in Figure 11, the MR signal was calculated for multiple contrast concentrations (Figure 17). The simulation shows a maximum value of the signal for a contrast concentration of 3.5mM. For signals with an intensity of <1.05, the contrast concentration can have two solutions. For example, for a signal intensity of 1, the concentration can be 1.5mM and 6mM. This indicates that Eq. [3] was not optimal to convert the signals into concentrations.

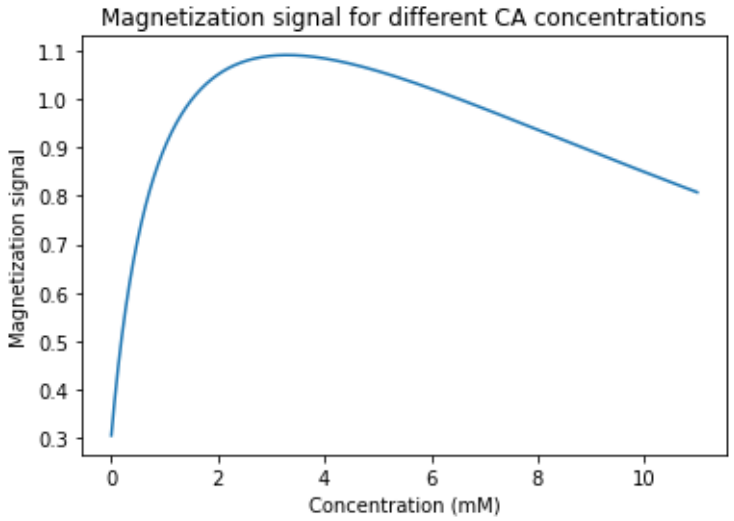

Figure 17. Magnetization signal described by Eq. [3] for different contrast concentrations (mM). The MR signal increases for lower concentrations, but the MR signal decreases for concentrations above 3.5mM.

Since the concentration curves generated with the signal Eq. [3] were abnormal, new concentration curves were generated with simplified equations of the signal (Eq. [1]) for a T1-weighted TFE sequence (Figure 18).

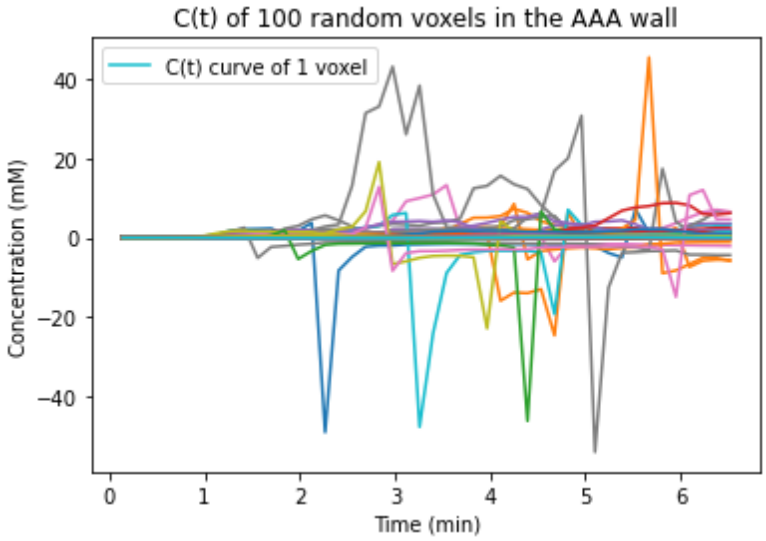

Figure 18. Concentration time curves (C(t)) calculated from signal intensity curves with Eq. [1] of one patient of 100 random voxels in the Abdominal Aorta Aneurysm (AAA) wall. Some concentration curves have extreme positive and negative outliers.

Evaluation of the generated concentration time course revealed several curves with extremely positive and negative concentration values for some timeframes. The signal time curves that resulted in these abnormal concentration curves were studied and these signals showed abnormal behavior as well. For example, the signal would get lower after the influx of CA. After removal of the abnormal concentration curves, only normally shaped curves remained (Figure 19). Around 10 percent of the total amount of concentration curves of the AAA wall were removed after applying the thresholds.

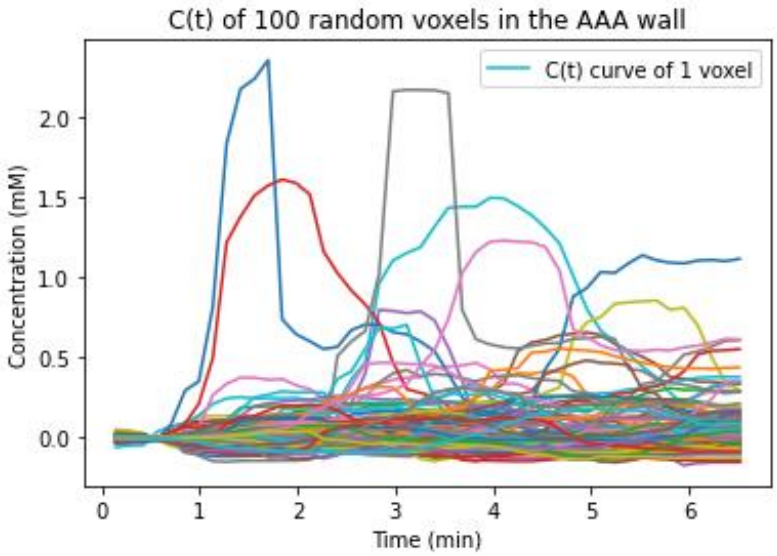

Figure 19. Concentration time curves (C(t)) calculated from signal intensity curves with Eq. [1] after removing outliers. The concentration curves of one patient of 100 random voxels in the Abdominal Aorta Aneurysm (AAA) wall are visualized.

5.4 K_{trans} perfusion maps

5.4.1 Qualitative results

To obtain parameter maps of K_{trans}, the generated concentration time curves were fitted to the ETofts model with the LSQ fitting method and the DCE-net. Figure 20 shows an axial slice of a K_{trans} map of one patient generated with the LSQ fitting method and the DCE-net. 3D visualization of K_{trans} maps of one patient for scan and rescan are visualized in Figure 21 for the LSQ fitting the DCE-net. In Appendix B, 3D K_{trans} maps of all patients that underwent two consecutive DCE-MRI scans are shown.

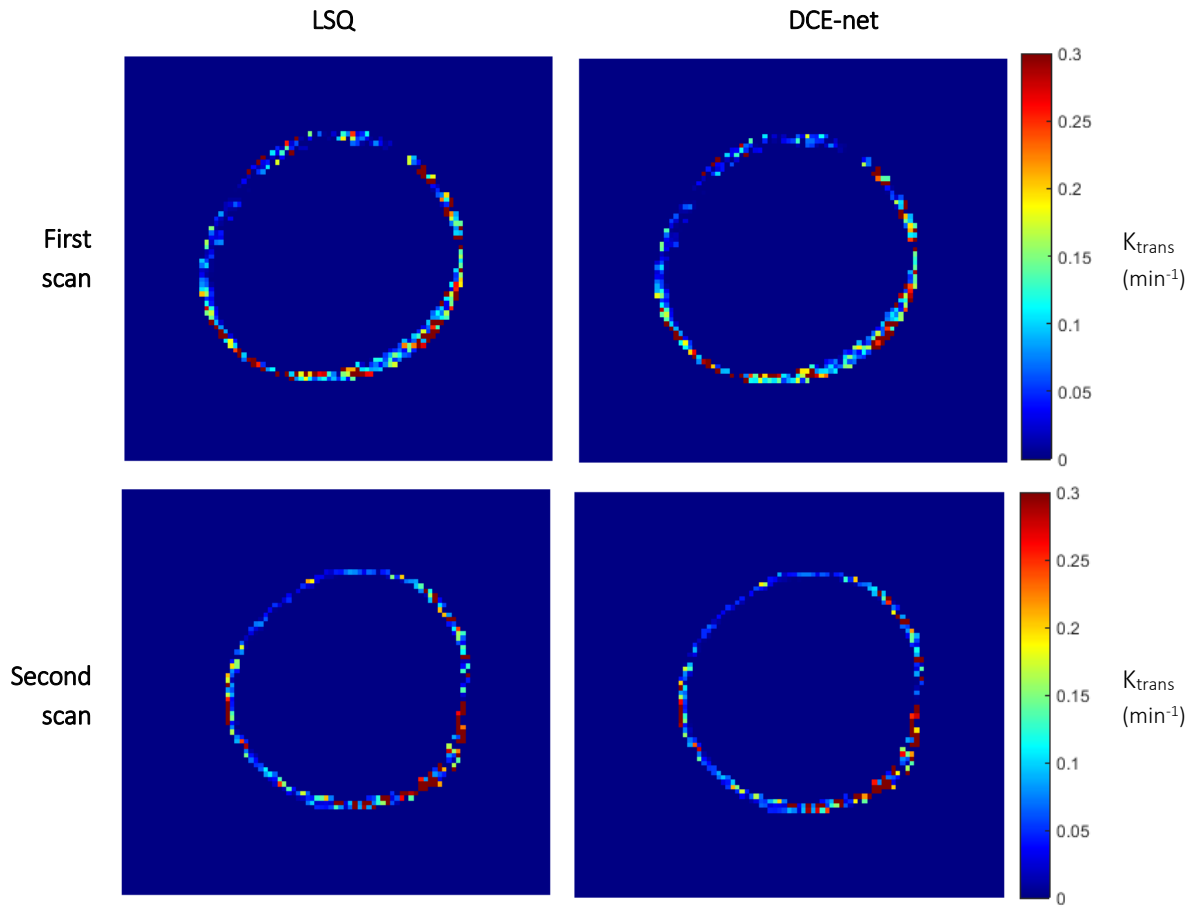

Figure 20. Axial intersection of K_{trans} maps of one patient of the first and second scan generated using the LSQ fitting and DCE-net. The colormap represents the value of K_{trans}, (min^{-1}). The K_{trans} maps generated with the LSQ fitting and DCE-net seem similar whereas the K_{trans} maps of the first and second scan are showing differences.

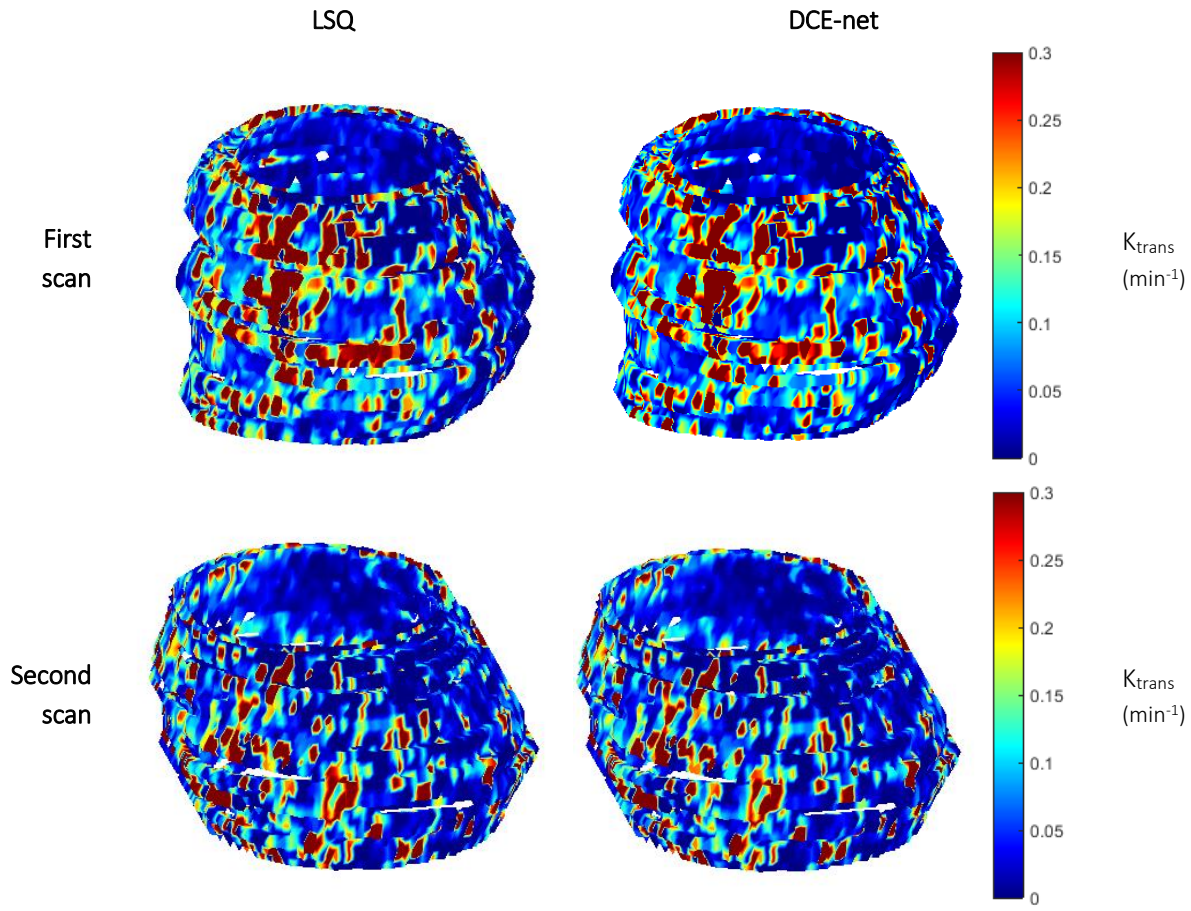

Figure 21. 3D K_{trans} maps one patient of the first and second scan generated with the LSQ fitting and DCE-net. The colormap represents the value of K_{trans}, (min^{-1}). The K_{trans} maps generated with the LSQ fitting and DCE-net seem similar whereas the K_{trans} maps of the first and second scan are showing differences.

5.4.2 Reproducibility K_{trans} maps

Correlation and Bland-Altman plots including CoV were generated for quantitative assessment of the reproducibility of mean K_{trans} of the small segments for both the LQS fitting and the DCE-net of all patients (Figure 22 and Figure 23). In Appendix C, the correlation and Bland-Altman plot of all segments for each patient separately are visualized.

The mean differences between the small segments of the K_{trans} maps of the first and second scan (blue lines in Figure 22 and Figure 23) were tested for significance for both methods. For the LSQ fitting method the mean difference of -0.05 min^{-1} was significant ($P<0.001$). The mean value of the difference of the K_{trans} maps calculated using the DCE-net was -0.04 min^{-1} ($P<0.001$).

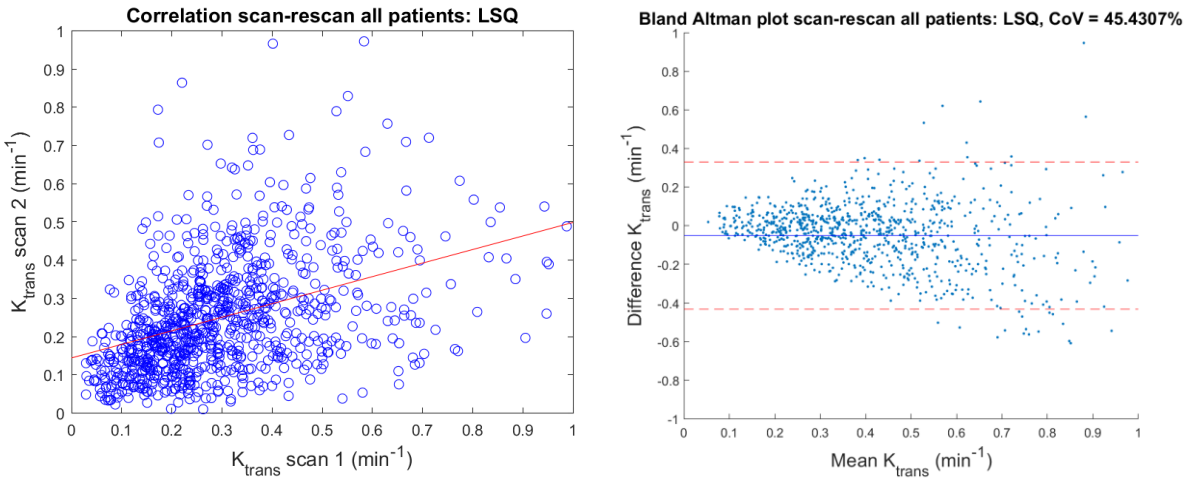

Figure 22. Correlation and Bland-Altman plots of the small segments for the LSQ method for all patients combined. Left: correlation plot of the first and second scan with the dots representing the median K_{trans} values (min^{-1}) of all small segments for all patients. Right: Bland-Altman plot with the blue dots representing the difference of the two K_{trans} values (first and second scan) for each small segment on the vertical axis and the average of the two K_{trans} values on the horizontal axis. The blue line is the average difference and the red dotted lines are the standard deviation of the K_{trans} values.

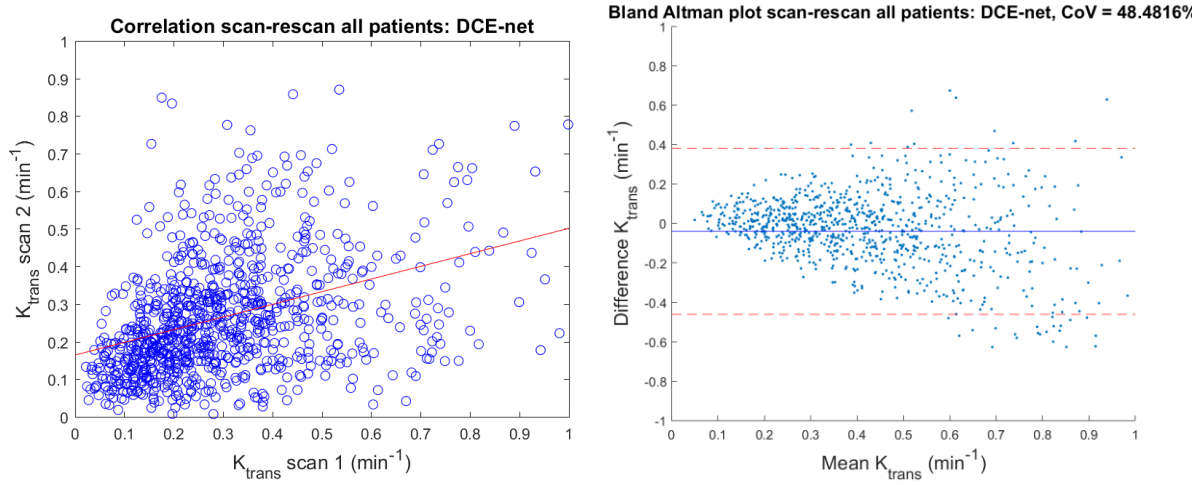

Figure 23. Correlation and Bland-Altman plots of the small segments for the DCE-net method for all patients combined. Left: correlation plot of the first and second scan with the dots representing the median K_{trans} values (min^{-1}) of all small segments for all patients. Right: Bland-Altman plot with the blue dots representing the difference of the two K_{trans} values (first and second scan) for each small segment on the vertical axis and the average of the two K_{trans} values on the horizontal axis. The blue line is the average difference and the red dotted lines are the standard deviation of the K_{trans} values.

Correlation and Bland-Altman plots of mean K_{trans} of the large segments of all patients together were generated for the LSQ fitting method (Figure 24). The same plots were generated for the DCE-net (Appendix C3) which had a CoV of 27.3%. The mean difference between the first and second scan was -0.05 min^{-1} ($P<0.001$ for the LSQ fitting method and -0.04 min^{-1} ($P<0.001$) for the DCE-net.

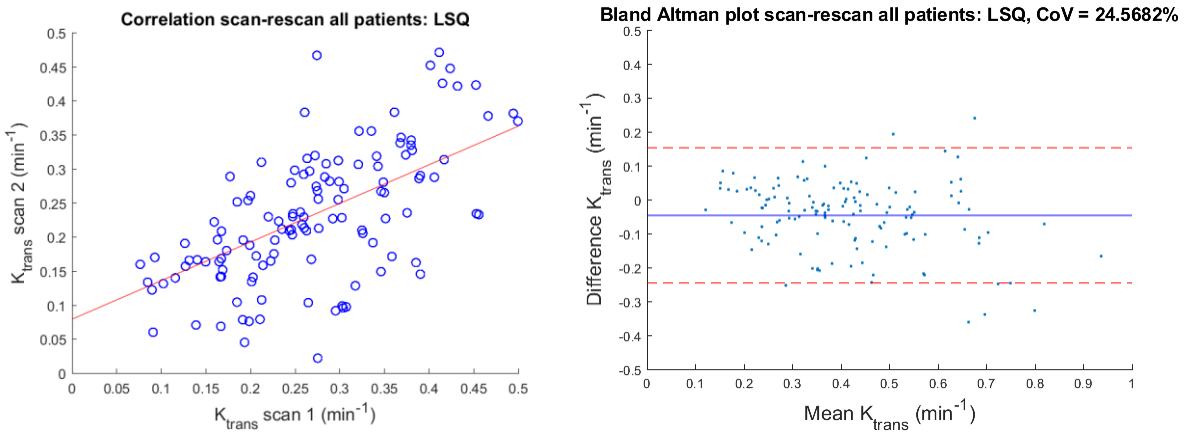

Figure 24. Correlation and Bland-Altman plots of the larger segments for the LSQ method for all patients combined. Left: correlation plot of the first and second scan with the dots representing the median K_{trans} values (min-1) of all large segments for all patients. Right: Bland-Altman plot with the blue dots representing the difference of the two K_{trans} values (first and second scan) for each larger segment on the vertical axis and the average of the two K_{trans} values on the horizontal axis. The blue line is the average difference and the red dotted lines are the standard deviation of the K_{trans} values.

The CoV for the analysis of the small AAA segments of the LSQ fitting method was 45.4% and 48.5% for the DCE-net. For the analysis of the large AAA segments, the CoV was 24.5% for the LSQ fitting method and 27.3% for the DCE-net. The mean differences between the first and second scan in both the small and large segments were -0.05 min^{-1} for the LSQ fitting method and -0.04 min^{-1} for the DCE-net. Thus, the difference between the methods is minimal. The K_{trans} maps generated by using the more established LSQ fitting method were used for clinical analysis.

Additional Bland-Altman plots were computed of K_{trans} maps generated with the LSQ fitting method. The following K_{trans} values were evaluated: median K_{trans} values of the whole annotated AAA, median K_{trans} values of the slices with maximal diameter, the 95th percentile K_{trans} values of the whole annotated AAA and the 95th percentile K_{trans} values of the slice with maximal AAA diameter (Figure 25). There was a fixed bias in the median and maximum K_{trans} values calculated in the AAA wall slice of the maximum diameter (Table 2). There was no fixed bias in the mean differences of median and maximum K_{trans} values of the complete annotated AAA wall.

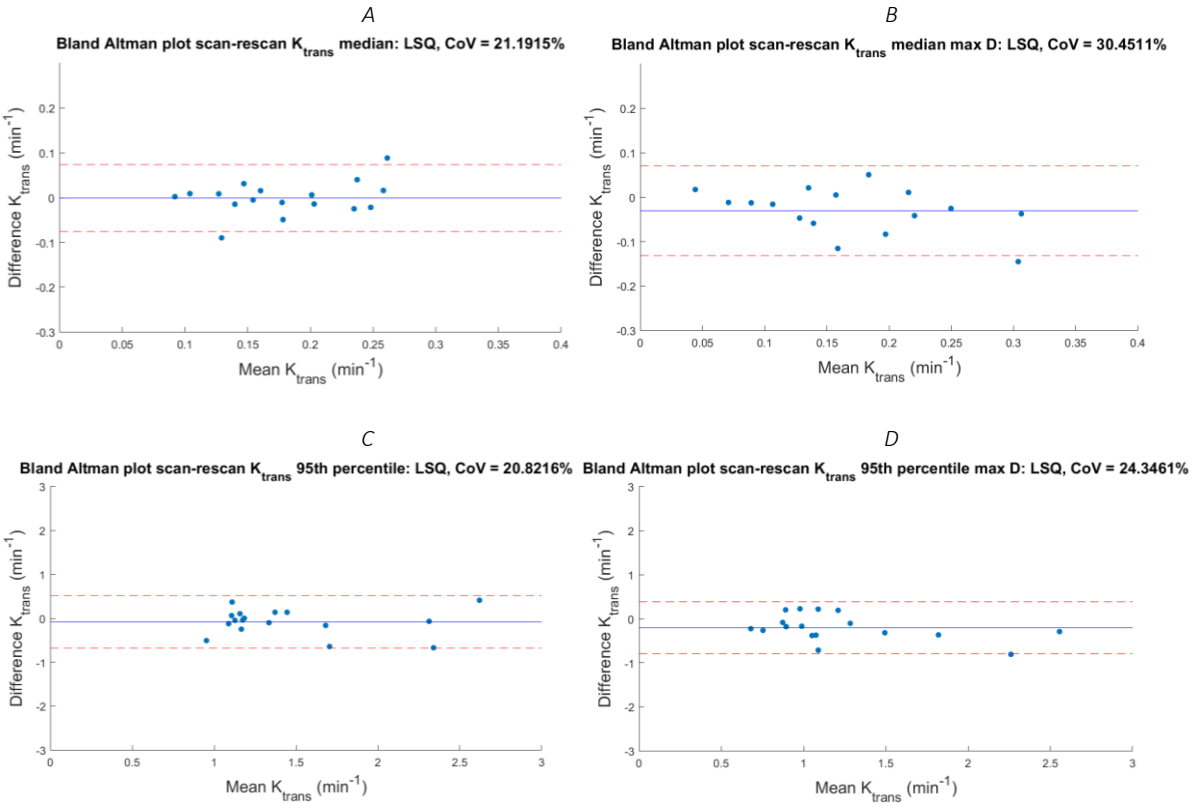

Figure 25. Bland-Altman plots of the LSQ fitting method for all patients combined for median and maximum K_{trans} values (min-1). The blue dots represent the difference of the two K_{trans} values (first and second scan) on the vertical axis and the average of the two K_{trans} values on the horizontal axis. In A) Median K_{trans} values of the whole annotated AAA, in B) the median K_{trans} values of the slices with maximal diameter, in C) the 95th percentile K_{trans} values of the whole annotated AAA, and in D) the 95th percentile K_{trans} values of the slice with maximal AAA diameter.

Table 2. The mean value of the differences between K_{trans} values (min-1) of the first and second scan, and the CoV of the median K_{trans} values of the whole annotated AAA, the median K_{trans} values of the slices with maximal diameter, the 95th percentile K_{trans} values of the whole annotated AAA, and the 95th percentile K_{trans} values of the slice with maximal AAA diameter. In case the difference was significant, there was a fixed bias (in red).

K_{trans} values	Difference rescan-scan (min^{-1}) (p-value)	CoV
Median K_{trans}	-0.00 (p = 0.94)	21.2%
Median K_{trans} slice maximum diameter	-0.03 (p = 0.03)	30.5%
95th percentile K_{trans} AAA	-0.08 (p = 0.30)	20.8%
95th percentile K_{trans} slice maximum diameter	-0.20 (p = 0.01)	24.3%

5.5 Clinical analysis K_{trans} maps

K_{trans} maps of scan and rescan generated with the LSQ fitting were correlated to clinical parameters. The clinical parameters were obtained from patients' files and DCE-MRI scans (Table 3). The mean imaging follow-up was 47.8 ± 22.7 months. In two patients there was a strong suspicion of a ruptured AAA as the cause of death. Several K_{trans} parameters were calculated from the 3D parameter maps of the AAA wall for all patients (Table 4).

Table 3. Diameters, mean and maximum growth, and rupture of the abdominal aortic aneurysm for all included patients. The mean imaging follow-up was 47.8 ± 22.7 months. Max = maximum, AP = anterior-posterior, US = ultrasound, N/A = not available.

Patient	Mean growth per year (mm)	Max growth in 1 year (mm)	Max AP US diameter at time of DCE-MRI scan (mm)	Max diameter DCE-MRI 1st scan (mm)	Max diameter DCE-MRI 2nd scan (mm)	Strong suspicion of ruptured AAA as cause of death
1	2.8	5.5	52.5	*N/A*	53.8	
2	5.4	*N/A*	62 (CTA)	69.8	70.1	
3	3.2	3.5	38	47.6	47.7	
4	1.8	2.0	55	61.0	62.6	
5	2.0	3.0	40	49.0	48.6	
6	4.0	3.0	49	55.6	55.6	
7	6.4	*N/A*	36	41.8	42.9	
8	1.8	4.0	45	*N/A*	51.3	
9	2.1	3.5	41	46.8	48.6	X
10	0.0	0.0	35	29.3	*N/A*	
11	*N/A*	*N/A*	*N/A*	38.4	36.7	
12	0.8	2.0	45	56.0	56.8	
13	0.8	2.5	48.5	55.9	56.0	
14	0.0	0.0	*N/A*	34.7	39.3	
15	4.0	4.0	50	60.2	60.9	
16	2.1	5.5	47	53.1	56.8	
17	3.6	6.0	59	63.8	66.1	
18	*N/A*	*N/A*	60 (CTA)	64.3	63.3	
19	1.4	2.0	52	57.7	58.8	
20	3.1	*N/A*	40	65.7	66.1	X

Table 4. Calculated K_{trans} values generated using the LSQ fitting method of the first and second scan for all patients that had clinical data. Median (med) K_{trans} (K_t) values of the whole annotated AAA, the median K_{trans} values of the slices with maximal (max) diameter (diam), the 95th percentile K_{trans} values of the whole annotated AAA, and the 95th percentile K_{trans} values of the slice with maximal AAA diameter. N/A = not available.

Patient	Scan 1				Scan 2			
	Med K_t AAA (min^{-1})	Med K_t max diam (min^{-1})	95th percentile K_t AAA (min^{-1})	95th percentile K_t max diam (min^{-1})	Med K_t AAA (min^{-1})	Med K_t max diam (min^{-1})	95th percentile K_t AAA (min^{-1})	95th percentile K_t max diam (min^{-1})
1	*N/A*	*N/A*	*N/A*	*N/A*	0.09	0.12	0.95	1.04
2	0.1	0.1	0.77	0.89	0.08	0.11	0.72	0.79
3	0.16	0.16	1.17	1.33	0.14	0.12	1.01	0.97
4	0.17	0.22	1.56	1.8	0.18	0.18	1.5	1.51
5	0.12	0.11	1.61	0.74	0.11	0.05	2.02	0.94
6	0.14	0.13	0.62	0.53	0.25	0.21	1.01	0.77
7	0.17	0.17	0.74	0.71	0.15	0.15	0.84	0.55
8	*N/A*	*N/A*	*N/A*	*N/A*	0.19	0.23	1.12	1.4
9	0.12	0.14	0.8	0.96	0.03	0.03	0.3	0.25
10	0.27	0.19	2.67	3.63	*N/A*	*N/A*	*N/A*	*N/A*
11	*N/A*	*N/A*	*N/A*	*N/A*	*N/A*	*N/A*	*N/A*	*N/A*
12	0.14	0.11	0.87	0.53	0.18	0.16	1.01	0.73
13	0.09	0.06	0.86	0.59	0.12	0.05	0.61	0.33
14	0.07	0.05	0.92	0.65	0.08	0.04	1.06	0.48
15	0.13	0.14	0.79	0.65	0.14	0.15	0.76	0.87
16	0.1	0.1	0.92	1.1	0.1	0.05	0.82	0.79
17	0.08	0.08	0.79	0.61	0.09	0.06	0.79	0.53
18	*N/A*	*N/A*	*N/A*	*N/A*	*N/A*	*N/A*	*N/A*	*N/A*
19	0.14	0.25	1.78	1.78	0.13	0.11	1.11	0.97
20	0.06	0.02	1.35	0.84	0.06	0.04	0.71	0.47

Pearson correlations of diameters and K_{trans} values were calculated for the first and second scan (Table 5). Pearson correlations of aneurysm growth and K_{trans} values were calculated for the first and second scan (Table 6). The K_{trans} maps were only correlated to diameter and AAA growth and not to aneurysm rupture. Only two patients had a ruptured AAA, and therefore, statistical analysis on this event could not be performed.

Table 5. Pearson correlation coefficients (R) of K_{trans} values vs. maximal anterior-posterior AAA diameter measured on ultrasound for the first and second scan. Both generated K_{trans} maps of the first and second scan were correlated to AAA growth. A significant correlation was marked red.

	R	p-value
Scan 1: AAA diameter (n = 16) vs.:		
Median K_{trans}	-0.51	0.04
Median K_{trans} slice maximum diameter	-0.20	0.45
95th percentile K_{trans} AAA	-0.38	0.14
95th percentile K_{trans} slice maximum diameter	-0.44	0.09
Scan 2: AAA diameter (n = 17) vs.:		
Median K_{trans} AAA	-0.02	0.93
Median K_{trans} slice maximum diameter	0.05	0.86
95th percentile K_{trans} AAA	-0.18	0.50
95th percentile K_{trans} slice maximum diameter	0.13	0.62

Table 6. Pearson correlation coefficients (R) for the first and second scan of K_{trans} values vs. mean AAA growth of a mean follow-up of 47.8 ± 22.7 months and vs. maximal AAA growth during this follow-up, both determined based on ultrasound data. Both generated K_{trans} maps of the first and second scan were correlated to AAA growth. A significant correlation was marked red.

	R	p-value
Scan 1: Mean growth per year (n = 16) vs.:		
Median K_{trans}	-0.10	0.72
Median K_{trans} slice maximum diameter	0.01	0.96
95th percentile K_{trans}	-0.51	0.05
95th percentile K_{trans} slice maximum diameter	-0.39	0.13
Scan 2 Mean growth per year (n = 17) vs.:		
Median K_{trans}	-0.08	0.76
Median K_{trans} slice maximum diameter	0.26	0.31
95th percentile K_{trans}	-0.23	0.49
95th percentile K_{trans} slice maximum diameter	-0.05	0.85
Scan 1: Maximum growth in one year (n = 13) vs.:		
Median K_{trans}	-0.42	0.15
Median K_{trans} slice maximum diameter	-0.23	0.44
95th percentile K_{trans}	-0.54	0.06
95th percentile K_{trans} slice maximum diameter	-0.46	0.11
Scan 2: Maximum growth in one year (n = 14) vs.:		
Median K_{trans}	-0.17	0.57
Median K_{trans} slice maximum diameter	-0.01	0.97
95th percentile K_{trans}	-0.27	0.36
95th percentile K_{trans} slice maximum diameter	0.07	0.82

Median K_{trans} of the whole annotated AAA of the first DCE-MRI scan and the AAA diameter measured on ultrasound had a significant correlation with an R-value of -0.51 [-0.8, -0.02] (P = 0.043) (Figure 26A). For the first scan, the correlation between the 95th percentile K_{trans} value of the whole annotated AAA and the mean growth per year was significant with an R-value of -0.51 [-0.8, -0.01] (P = 0.045) (Figure 26B).

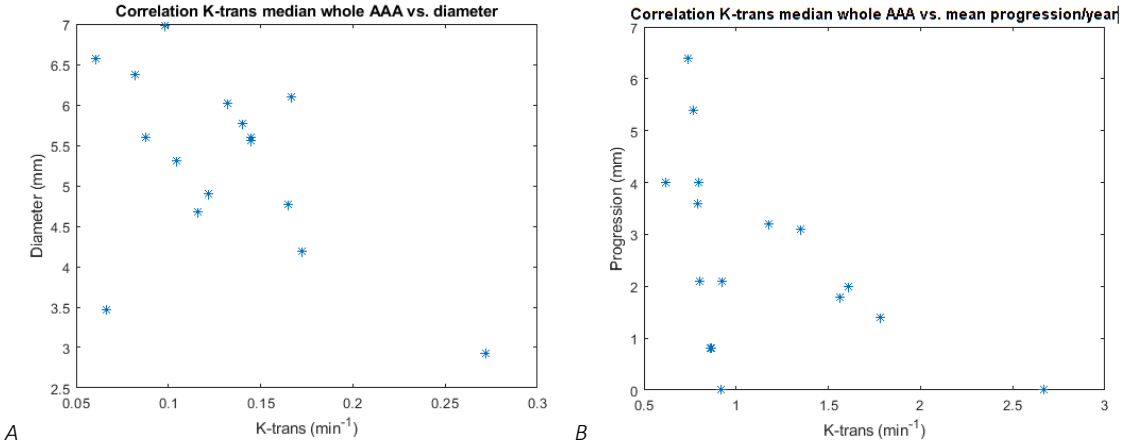

A B

Figure 26. (A) Scatterplot of AAA diameter vs. median K_{trans} of the whole AAA with a Pearson R-value of -0.51 (P = 0.043). (B) Scatterplot of mean AAA growth per year vs. median K_{trans} of the whole AAA with a Pearson R-value of -0.51 (P = 0.045).

6 Discussion

In this thesis, several experiments and simulations were performed to give insight into the optimal method to calculate K_{trans} by using 3D DCE-MRI data of AAAs. The K_{trans} maps were successfully generated by using both the LSQ fitting method and the DCE-net and had a moderate reproducibility. Furthermore, the K_{trans} maps were correlated to clinical parameters but this analysis could not yet determine the clinical value of the biomarker K_{trans}.

Bland-Altman plots of both methods showed moderate scan-rescan reproducibility. Both fitting methods had a fixed bias of -0.05 (LSQ fitting) and -0.04 (DCE-net) for the large and small segments. Consequently, K_{trans} values of the first scan were higher compared to K_{trans} values of the second scan. It remains unclear why this systematic error appeared. One explanation could be that extreme K_{trans} values may have a large effect on the median K_{trans} value of specific regions. Also, in these plots multiple segments of the same patients are included and thus correlated measurements are included in this plot. Moreover, other factors can influence the scan-rescan reproducibility of the K_{trans} maps. For instance, an increased blood flow during the first scan due to anxiety of the patients may influence the outcome of the parameter map. However, when comparing the median K_{trans} values of the whole annotated AAA wall of scan and rescan, no fixed bias was found. Consequently, the overall K_{trans} maps were reproducible.

Furthermore, CoV was 45.4% for the LSQ fitting method and 48% for the DCE-net while comparing small K_{trans} segments of scan and rescan. In large K_{trans} segments, CoV were 24% and 27% the LSQ fitting and DCE-net, respectively. Thus, the K_{trans} maps are more robust for larger areas. While visually comparing the 3D K_{trans} maps, the overall high and low K_{trans} regions of the AAA wall are equal for scan and rescan.

The estimated AAA wall K_{trans} parameter maps of the deep learning method (DCE-net) were comparable to the conventional LSQ fitting method. Moreover, both methods used a LSQ fitting of the ETofts model, therefore, similar outcomes can be expected. The small difference between the two fitting methods may be caused by the generalization of the DCE-net since the network is trained using all concentration curves of all patients. For this application, the DCE-net might not be solving handling the noisy data.

Although K_{trans} maps were only moderately reproducible, first attempts were made to correlate K_{trans} and clinical parameters. Median K_{trans} values of the first scan, generated using the LSQ fitting method, showed a moderate negative correlation with aneurysm diameter. Besides, the 95th percentile K_{trans} value of the first scan showed a moderate negative correlation with mean aneurysm growth. In other words, a large AAA diameter and more AAA growth were correlated with lower K_{trans} values which indicates less perfusion of the AAA wall. These results are in line with the hypothesis that a low microvasularisation, and thus more hypoxia, would weaken the aortic wall. In contrast, our findings do not correspond to the results of Nguyen et al. (5) who have quantified K_{trans} of the AAA in a limited amount of 2D axial slices. In their study, they found a moderate positive correlation between aneurysm diameter and K_{trans}, meaning a higher perfusion in larger diameters. However, their 2D K_{trans} maps of the 3D aneurysm wall may not capture all important information compared to our generated 3D K_{trans} maps. Nonetheless, our findings do not confirm the hypothesis that an increased microvascularization weakens the aortic wall and causes rupture.

The correlations of K_{trans} values and clinical parameters were only significant for the first scans and not for the K_{trans} maps of the second scan. Different patients were included in the clinical K_{trans} analysis of the first and second scan, which could explain the difference in outcome for the first and second scan. Nonetheless, calculated K_{trans} values had a large variability and were not consistent which may have caused the moderate reproducibility of the generated K_{trans} maps.

The first step in obtaining the K_{trans} parameter maps was the conversion of signal to concentration curves. It is of major importance that this step is executed accurately. Therefore, the conversion of signal to concentration curves was simulated in order to understand and find a solution for the abnormal thresholded curves shown in Figure 11. The behavior of the signal for high concentrations could be explained by the effect of the added iMSDE and fat saturation pulses. Signal Eq. [3] corrected for the additional T2 weighting that occurs because black-blood pulses were applied. However, the T2 weighting might be a too large effect for high concentrations which causes the signal to decrease after the maximum value of 3.5mM CA. Thus, the incoming contrast will decrease longitudinal (T1) relaxation time resulting in an increase of the MR signal. On the other hand, incoming contrast will decrease transverse (T2) relaxation time resulting in less signal. Consequently, the signal increases with inflow of contrast, to a maximum value of 3.5mM, and then decreases due to the T2 effect when even more contrast arrives.

In order to obtain normally shaped concentration curves, solving this T2 effect must be further explored. In this study, the T2 effect was omitted by using another simplistic signal equation (Eq. [1]) which ignores the effect of T2 relaxation. Nonetheless, Eq. [3] describes the underlying physical phenomenon better but does not generate realistic concentration curves, and therefore further investigation is designated.

6.1 Limitations

In the process of estimating the aortic wall perfusion, multiple simplifications were made. One important simplification is the used signal equation (Eq. [1]) to convert the signal to concentration time curves. This equation does not take the T2 relaxation into account while it is present in the scans because of the black blood and fat suppression pulses. Therefore, estimated concentrations might not correlate with the actual concentrations in the voxels. Moreover, this new signal equation still resulted in some abnormal concentration curves with several outliers. Signal time curves of these abnormal concentration time curves were studied and showed a signal decrease following contrast arrival. Hence, concentration time curves cannot show normal behavior when the input signal is already abnormal. All outliers were removed and excluded from further analyses. In the final concentration curves, a substantial number of curves had values below zero, which may be caused by noise, breathing artifacts, movement of the patient and pulsatile movement of the aorta itself. Taking it all together, the accuracy of the obtained concentration curves, which were used to calculate K_{trans} maps, can be questioned and it remains unclear to what extent the calculated curves describe the actual concentrations of contrast agent in each voxel.

Furthermore, the selection of AAA wall voxels has some pitfalls. The masks are annotated slice by slice on the DCE-MRI scans which have poor quality and poor resolution. An annotation that is slightly off could mean the voxels located adjacent to the AAA wall are included in the analyses. Consequently, including these voxels has a direct effect on the calculated K_{trans} values. A systemic difference in AAA wall annotations could influence the scan-rescan reproducibility of K_{trans} maps.

Moreover, the selected voxels may not all have sufficient contrast enhancement. The signal enhancement of the DCE-MRI images was visually inspected (Figure 16). This figure illustrates that the annotated AAA wall (in green) does not have a high signal enhancement for every voxel (Figure 16 A, B) since only the voxels in

yellow have a high signal enhancement. Other than a poor microvasularisation status, low enhancement may be caused by wrong timing of contrast injections, movement of the aorta itself, or breathing artifacts. However, some causes for inaccurate selection of AAA wall voxels such as the relatively low resolution and breathing artifacts were hard to overcome.

For the clinical analysis, thirteen to seventeen patients could be included, which is a relatively small group to perform adequate statistical analyses on. Thus, outliers may have a large effect on the results of this study. Another relevant remark for the current clinical analysis is the simplification of the 3D K_{trans} maps into one K_{trans} value considering the substantial part of the 3D parameter map that is lost. Moreover, AAA progression was calculated based on diameters measured on surveillance ultrasound imaging. This imaging technique is prone to observer errors. Furthermore, the diameters measured on ultrasound and calculated based on the annotated DCE-MRI scans differ. Explanations for this difference could be the use of different techniques and the measurement in the anterior-posterior direction on ultrasound and maximal diameter measurement on axial slices on DCE-MRI.

6.2 Recommendations

The first recommendation is to perform new DCE-MRI scans to improve the scanning protocol and to obtain more patient data. MRI scanning techniques have been improved over the last years and scanning with a higher resolution would improve the quantification of K_{trans}, especially for the relatively thin AAA wall. More sequential patient data would improve reliability of clinical outcomes.

6.2.1 Technical recommendations

One essential step that needs to be improved is the conversion of the MR signal to concentration time curves. Most importantly, the conversion of the signal into concentration must be more robust. Therefore, the signal equation that describes the MR signal should be adjusted to better match the actual MR signal. Also, the MRI sequence itself can be altered to minimize the T2-effect, or the amount of injected contrast agent could be lowered to also minimize the T2-effect.

In this thesis, multiple assumptions were made in the process of estimating the aortic wall perfusion. A fixed value from literature was used for the T10 relaxation time. The conversion of signal to concentration is dependent on the tissue's T10 time and, consequently, variation in T10 may have a considerable effect on the parameter map values. (35) Furthermore, a fixed AIF from literature was used which is equal for all patients. However, the AIF can be measured for each patient to make the K_{trans} maps more patient specific. Patient-variable T10 times and AIFs must be measured accurately otherwise it may cause patient heterogeneity. (47)

The DCE-net may still be a promising method to perform PK modeling and obtain parameter maps. However, it still needs improvement. The network could be trained with more data. Also, the architecture of the network and amount of layers could be optimized. Furthermore, deep learning methods are being developed whereby spatial information can be taken into account (42). This could be an improvement for deep learning methods to become more robust against outliers. Moreover, deep learning networks may omit the necessity of the conversion of signal to contrast time curve. Recently, deep learning models are investigated to go from signal images directly to parameter maps. (48)

Additional analyses can be performed to assess the calculation of $K_{trans.}$ For example, the reproducibility of the other fitting parameters k_{ep}, dt, v_e, v_p can be evaluated for reproducibility so it could make a more robust

assessment of the fitting methods. Also, the parameter maps of the LSQ fitting method and the DCE-net can be compared voxel-wise to assess the agreement of the two methods.

6.2.2 Clinical recommendations

In future scans, the field of view could be extended to visualize the whole aneurysm and a healthy part of the aorta. However, the temporal resolution must be retained. When the field of view could be increased, the K_{trans} of a healthy aorta and sick aorta in the same patient can be compared. This ratio may be a better indication of the severity of the disease per patient.

Furthermore, the current clinical analysis could be extended. In this study, median and maximum K_{trans} values of the whole 3D AAA wall were calculated. This is a crucial simplification of the detailed 3D K_{trans} map. Therefore, a clinical analysis of smaller regions of the AAA wall may indicate weakened spots of the vessel wall. For example, the mean K_{trans} value of the large regions such as the segments illustrated in Figure 15. The maximal and minimal K_{trans} of these areas could be compared with clinical parameters such as diameter, progression and rupture. In case sequential DCE-MRI scans are performed with, for instance, a one-year interval, the K_{trans} values of each segment could be analyzed and compared with progression.

Also, K_{trans} can be compared with intraluminal thrombus. Thrombus in the AAA is a source of inflammatory cells and may have a relation with the progression of AAAs (49, 50). Therefore, it would be interesting to correlate K_{trans} of the AAA wall to the local thrombus thickness. To correlate thrombus thickness with $K_{trans,}$ the AAA wall can be divided into the large segments such as the segments illustrated in Figure 15. Mean or median K_{trans} values of these segments can then be correlated to the thrombus thickness of this segment.

Finally, the relation between K_{trans} and aneurysm progression needs to be investigated. More patients need to be scanned to obtain more results of the relation of K_{trans} with AAA diameter, AAA growth and rupture. Earlier histological research by Holmes et al. (24) showed that the microvascularisation was high in aneurysms. Besides, 2D DCE-MRI analysis of Nguyen et al. (5) showed a high K_{trans} (high perfusion) was moderately correlated with aneurysm diameter. However, other hypotheses suggest that ischemia of the AAA wall and hypoxia might also cause weakening of the aneurysm wall. (26, 27) More clinical analyses are required to determine the relationship between the perfusion of the AAA wall and AAA progression and risk of rupture.

7 Clinical evaluation and future perspective

Currently, there is no reliable measurement to predict which patient has a stable AAA and which aneurysms are more likely to rupture, and consequently, these people are living in great uncertainty. Aneurysm diameter is currently the best measure to indicate the risk of AAA rupture. However, solely aneurysm diameter is not sufficient and further investigation is needed. Functional biomarkers can offer valuable information regarding physiological processes in the pathogenesis of the dilated aorta.

K_{trans} is a promising biomarker that is a measure of the perfusion of the aortic wall (5). In this thesis, steps were taken to improve DCE-MRI modeling for AAA patients. New insights into the equations to use for signal to concentration conversion are of major importance for further research. Performed analyses and experiments were in line with the MARVY project and the methods will be continued within this project. However, the results of this thesis brought up some pitfalls of 3D DCE-MRI imaging for the AAA wall, especially the scanning protocol and conversion from signal to concentration time curve still needs improvement. When the K_{trans} maps will be more robust, clinical analysis can be extended.

Therefore, an additional optimization phase before scanning AAA patients will be incorporated into the MARVY project. In this optimization phase, the MRI sequence will be optimized as well as the models to convert the signal to concentration. Also, the contrast injection protocol may be revised and the DCE-net may be improved. After performing these optimizations, AAA patients will undergo DCE-MRI scans and the clinical impact of K_{trans} can be investigated.

For now, clinical analysis could not give insight into the use of K_{trans} as a biomarker for AAA progression and rupture yet. The calculated 3D K_{trans} maps were moderately reproducible and many simplifications and assumptions were made in the process. Nonetheless, the ability to generate the 3D K_{trans} maps offers great potential for clinical analysis of the microvascular status of the whole AAA wall. For further research, the clinical value of K_{trans} should be analyzed in more detail. The thrombus analysis could give insight into the correlation between thrombus and the microvascular status of the AAA wall. Also, the 3D map can be divided into large segments to identify weakened regions of the aneurysm.

Potentially, if K_{trans} would be a biomarker that could be used in addition to the AAA diameter, patients with an AAA can have more certainty regarding the progression and rupture risk of their AAA. Consequently, a more considered decision for repair of the AAA can be made. Some patients with a relatively small diameter aneurysm will then receive treatment while some patients with a large AAA diameter but a low risk of rupture only need surveillance. Therefore, the incorporation of functional imaging biomarkers may change current standard of practice for AAA patients.

8 Conclusion

K_{trans}, which represents the microvascular status of the aneurysm wall, might be a valuable biomarker to predict aneurysm progression and risk of rupture. In this thesis, we were able to quantify K_{trans} on 3D DCE-MRI using two methods to perform parametric fitting of the Etofts PK model. However, the methods to generate the 3D K_{trans} maps must be improved. Now, the derived parameter maps from DCE-MRI data were sensitive to acquisition and post-processing techniques. Nonetheless, the analyzed fitting methods, the LSQ and DCE-net, both generated moderately reproducible K_{trans} maps. The DCE-net did not outperform the LSQ fitting. The generated 3D K_{trans} maps were more robust in larger regions compared to smaller regions. Furthermore, the clinical use of K_{trans} as a biomarker for progression and rupture could not yet be determined based on the results of this thesis. Therefore, an optimization phase will be added to the MARVY project to determine whether K_{trans} could be a valuable biomarker in the treatment of AAAs.

References

1. Wanhainen A, Verzini F, Van Herzeele I, Allaire E, Bown M, Cohnert T, et al. Editor's Choice - European Society for Vascular Surgery (ESVS) 2019 Clinical Practice Guidelines on the Management of Abdominal Aorto-iliac Artery Aneurysms. Eur J Vasc Endovasc Surg. 2019;57(1):8-93.

2. Parkinson F, Ferguson S, Lewis P, Williams IM, Twine CP. Rupture rates of untreated large abdominal aortic aneurysms in patients unfit for elective repair. Journal of vascular surgery. 2015;61(6):1606-12.

3. Groeneveld ME, Meekel JP, Rubinstein SM, Merkestein LR, Tangelder GJ, Wisselink W, et al. Systematic Review of Circulating, Biomechanical, and Genetic Markers for the Prediction of Abdominal Aortic Aneurysm Growth and Rupture. Journal of the American Heart Association. 2018;7(13).

4. Ahmed Z, Levesque IR. An extended reference region model for DCE-MRI that accounts for plasma volume. NMR in Biomedicine. 2018;31(7):e3924-e.

5. Nguyen VL, Backes WH, Kooi ME, Wishaupt MCJ, Hellenthal FAMVI, Bosboom EMH, et al. Quantification of abdominal aortic aneurysm wall enhancement with dynamic contrast-enhanced MRI: Feasibility, reproducibility, and initial experience. Journal of Magnetic Resonance Imaging. 2014;39(6):1449-56.

6. Wang N, Christodoulou AG, Xie Y, Wang Z, Deng Z, Zhou B, et al. Quantitative 3D dynamic contrast-enhanced (DCE) MR imaging of carotid vessel wall by fast T1 mapping using Multitasking. Magnetic resonance in medicine. 2019;81(4):2302-14.

7. Gezondheidsraad N. Incidentie, mortaliteit en prevalentie AAA in Nederland. Achtergronddocument bij het advies Bevolkingsonderzoek naar aneurysma van de abdominale aorta (AAA). Achtergronddocument bij het advies Bevolkingsonderzoek naar aneurysma van de abdominale aorta (AAA). 2019:2-15.

8. Sakalihasan N, Limet R, Defawe OD. Abdominal aortic aneurysm. Elsevier B.V.; 2005. p. 1577-89.

9. Duong WQ, Fujitani RM, Grigorian A, Kabutey NK, Kuo I, de Virgilio C, et al. Evolving Utility of Endovascular Treatment of Juxtarenal, Pararenal, and Suprarenal Abdominal Aortic Aneurysms Associated With Increased Risk of Mortality Over Time. Annals of Vascular Surgery. 2021;71:428-36.

10. Mascia D, Grandi A, Porcellato L, Bertoglio L, Kahlberg A, Baccellieri D, et al. Open Repair of Pararenal Aneurysms: Renal Vessel Surgical Management. Springer International Publishing; 2019. p. 29-43.

11. Lee A, Dake MD. Abdominal and thoracic aortic aneurysms. Springer International Publishing; 2018. p. 197-207.

12. Filardo G, Powell JT, Martinez MA-M, Ballard DJ. Surgery for small asymptomatic abdominal aortic aneurysms. The Cochrane database of systematic reviews. 2015;2015(2):CD001835-CD.

13. Powell JT, Sweeting MJ, Ulug P, Blankensteijn JD, Lederle FA, Becquemin JP, et al. Meta-analysis of individual-patient data from EVAR-1, DREAM, OVER and ACE trials comparing outcomes of endovascular or open repair for abdominal aortic aneurysm over 5 years. Br J Surg. 2017;104(3):166-78.

14. Zankl H Schumacher U Krumsdorf H A Katus L Jahn C P Tiefenbacher AR, Zankl AR, Krumsdorf U, Katus L Jahn HA, Christiane Tiefenbacher mP, Schumacher H. Pathology, natural history and treatment of abdominal aortic aneurysms. Clin Res Cardiol. 2007;96:140-51.

15. Leurs LJ, Kievit J, Dagnelie PC, Nelemans PJ, Buth J. Influence of Infrarenal Neck Length on Outcome of Endovascular Abdominal Aortic Aneurysm Repair. Journal of Endovascular Therapy. 2006;13(5):640-8.

16. Daye D, Walker TG. Complications of endovascular aneurysm repair of the thoracic and abdominal aorta: Evaluation and management. AME Publishing Company; 2018. p. S138-S56.

17. Hiatt MD, Rubin GD. Surveillance for endoleaks: how to detect all of them. Seminars in vascular surgery. 2004;17(4):268-78.

18. Gleason TG. Endoleaks After Endovascular Aortic Stent-Grafting: Impact, Diagnosis, and Management. Seminars in Thoracic and Cardiovascular Surgery. 2009;21(4):363-72.

19. Bley T, Roos J. Pre- and Post-aortic Endovascular Interventions: What a Radiologist Needs to Know. Springer; 2019. p. 215-22.

20. Barkhausen J, Kahn T, Krombach GA, Kuhl CK, Lotz J, Maintz D, et al. White Paper: Interventional MRI: Current Status and Potential for Development Considering Economic Perspectives, Part 1: General Application. RoFo : Fortschritte auf dem Gebiete der Rontgenstrahlen und der Nuklearmedizin. 2017;189(7):611-23.

21. Abdelaziz MEMK, Tian L, Hamady M, Yang G-Z, Temelkuran B. X-ray to MR: the progress of flexible instruments for endovascular navigation. Progress in Biomedical Engineering. 2021;3(3):032004-.

22. Haynes H, Holmes W. The Emergence of Magnetic Resonance Imaging (MRI) for 3D Analysis of Sediment Beds. 2013.

23. Burris NS, Hope MD. 4D flow MRI applications for aortic disease. Magnetic resonance imaging clinics of North America. 2015;23(1):15-23.

24. Holmes DR, Liao S, Parks WC, Thompson RW. Medial neovascularization in abdominal aortic aneurysms: a histopathologic marker of aneurysmal degeneration with pathophysiologic implications. Journal of vascular surgery. 1995;21(5):761-2.

25. Choke E, Thompson MM, Dawson J, Wilson WRW, Sayed S, Loftus IM, et al. Abdominal aortic aneurysm rupture is associated with increased medial neovascularization and overexpression of proangiogenic cytokines. Arteriosclerosis, thrombosis, and vascular biology. 2006;26(9):2077-82.

26. Bruijn LE, van Stroe Gómez CG, Curci JA, Golledge J, Hamming JF, Jones GT, et al. A histopathological classification scheme for abdominal aortic aneurysm disease. JVS-Vascular Science. 2021;2:260-73.

27. Vorp DA, Lee PC, Wang DHJ, Makaroun MS, Nemoto EM, Ogawa S, et al. Association of intraluminal thrombus in abdominal aortic aneurysm with local hypoxia and wall weakening. Journal of Vascular Surgery. 2001;34(2):291-9.

28. DCE Parameters - Magnetism - Questions and Answers in MRI [Available from: https://www.mriquestions.com/dce-tissue-parmeters.html.

29. Gordon Y, Partovi S, Müller-Eschner M, Amarteifio E, Bäuerle T, Weber M-A, et al. Dynamic contrast-enhanced magnetic resonance imaging: fundamentals and application to the evaluation of the peripheral perfusion. Cardiovascular diagnosis and therapy. 2014;4(2):147-64.

30. Yankeelov TE, Gore JC. Dynamic Contrast Enhanced Magnetic Resonance Imaging in Oncology: Theory, Data Acquisition, Analysis, and Examples. Current medical imaging reviews. 2009;3(2):91-107.

31. Nguyen VL, Kooi ME, Backes WH, van Hoof RHM, Saris AECM, Wishaupt MCJ, et al. Suitability of Pharmacokinetic Models for Dynamic Contrast-Enhanced MRI of Abdominal Aortic Aneurysm Vessel Wall: A Comparison. PLoS ONE. 2013;8(10).

32. Jahng G-H, Li K-L, Ostergaard L, Calamante F. Perfusion Magnetic Resonance Imaging: A Comprehensive Update on Principles and Techniques. Korean J Radiol. 2014;15(5):554-77.

33. Wake N, Chandarana H, Rusinek H, Fujimoto K, Moy L, Sodickson DK, et al. Accuracy and precision of quantitative DCE-MRI parameters: How should one estimate contrast concentration? Magnetic resonance imaging. 2018;52:16-23.

34. Qi H, Huang F, Zhou Z, Koken P, Balu N, Zhang B, et al. Large coverage black-bright blood interleaved imaging sequence (LaBBI) for 3D dynamic contrast-enhanced MRI of vessel wall. Magn Reson Med. 2018;79(3):1334-44.

35. Heye T, Boll DT, Reiner CS, Bashir MR, Dale BM, Merkle EM. Impact of precontrast T10 relaxation times on dynamic contrast-enhanced MRI pharmacokinetic parameters: T10 mapping versus a fixed T10 reference value. J Magn Reson Imaging. 2014;39(5):1136-45.

36. Cárdenas-Rodríguez J, Howison CM, Pagel MD. A linear algorithm of the reference region model for DCE-MRI is robust and relaxes requirements for temporal resolution. Magnetic resonance imaging. 2013;31(4):497-507.

37. Parker GJM, Roberts C, Macdonald A, Buonaccorsi GA, Cheung S, Buckley DL, et al. Experimentally-derived functional form for a population-averaged high-temporal-resolution arterial input function for dynamic contrast-enhanced MRI. Magnetic Resonance in Medicine. 2006;56(5):993-1000.

38. Rata M, Collins DJ, Darcy J, Messiou C, Tunariu N, Desouza N, et al. Assessment of repeatability and treatment response in early phase clinical trials using DCE-MRI: comparison of parametric analysis using MR- and CT-derived arterial input functions. European Radiology. 2016;26(7):1991-8.

39. Chen H, Li F, Zhao X, Yuan C, Rutt B, Kerwin WS. Extended graphical model for analysis of dynamic contrast-enhanced MRI. Magn Reson Med. 2011;66(3):868-78.

40. Ulas C, Das D, Thrippleton MJ, Valdés Hernández MdC, Armitage PA, Makin SD, et al. Convolutional Neural Networks for Direct Inference of Pharmacokinetic Parameters: Application to Stroke Dynamic Contrast-Enhanced MRI. Frontiers in Neurology. 2019;9.

41. Yankeelov TE, Luci JJ, Lepage M, Li R, Debusk L, Lin PC, et al. Quantitative pharmacokinetic analysis of DCE-MRI data without an arterial input function: a reference region model. Magnetic Resonance Imaging. 2005;23(4):519-29.

42. Ottens T, Barbieri S, Orton MR, Klaassen R, van Laarhoven HWM, Crezee H, et al. Deep learning DCE-MRI parameter estimation: Application in pancreatic cancer. Medical Image Analysis. 2022;80:102512.

43. Zou J, Balter JM, Cao Y. Estimation of pharmacokinetic parameters from DCE-MRI by extracting long and short time-dependent features using an LSTM network. Med Phys. 2020;47(8):3447-57.

44. Hochreiter S, Schmidhuber J. Long Short-Term Memory. Neural Computation. 1997;9(8):1735-80.

45. Cho K, Merrienboer Bv, Bahdanau D, Bengio Y, editors. On the Properties of Neural Machine Translation: Encoder–Decoder Approaches. SSST@EMNLP; 2014.

46. Shen Y, Goerner FL, Snyder C, Morelli JN, Hao D, Hu D, et al. T1 relaxivities of gadolinium-based magnetic resonance contrast agents in human whole blood at 1.5, 3, and 7 T. Invest Radiol. 2015;50(5):330-8.

47. Huang W, Chen Y, Fedorov A, Li X, Jajamovich GH, Malyarenko DI, et al. The Impact of Arterial Input Function Determination Variations on Prostate Dynamic Contrast-Enhanced Magnetic Resonance Imaging Pharmacokinetic Modeling: A Multicenter Data Analysis Challenge. Tomography. 2016;2(1):56-66.

48. Nalepa J, Ribalta Lorenzo P, Marcinkiewicz M, Bobek-Billewicz B, Wawrzyniak P, Walczak M, et al. Fully-automated deep learning-powered system for DCE-MRI analysis of brain tumors. Artif Intell Med. 2020;102:101769.

49. Sagan A, Mrowiecki W, Mikolajczyk TP, Urbanski K, Siedlinski M, Nosalski R, et al. Local inflammation is associated with aortic thrombus formation in abdominal aortic aneurysms. Relationship to clinical risk factors. Thromb Haemost. 2012;108(5):812-23.

50. Łukasiewicz A, Garkowski A, Rutka K, Janica J, Łebkowska U. Evaluation of the thrombus of abdominal aortic aneurysms using contrast enhanced ultrasound - preliminary results. Scientific Reports. 2016;6(1):34152.

Appendix

A MRI specific parameters

Table A1. Scan specific inputs for signal to concentration conversion for the TFE sequence.

Parameter	Value
T10 (34)	1.150 s
T20 (34)	0.054 s
Repetition time	7.37e-3 s
Flip angle	11 degrees
T1 relaxivity Gadovist	4.5 mM
T2 relaxivity Gadovist	5.09 mM
# baseline scans	5

Table A2. Scan specific inputs for signal to concentration conversion for the FFE sequence.

Parameter	Value
T10 = 1.150	1.150 s
Repetition time	7.377e-3 s
Flip angle	11 degrees
T1 relaxivity Gadovist (46)	5 mM
# baseline scans	5

B 3D K_{trans} maps all patients

In the following sections the 3D K_{trans} maps are visualized for all patients that underwent consequetive DCE-MRI scans. The right K_{trans} maps are the first scans and the left maps are the second scans. Patients 1, 8 and 10 are left out because they only underwent one succesfull scan.

B.1 Patient 2

3D K_{trans} maps generated with LSQ fitting method. The color scale represents the value of K_{trans} in min^{-1}.

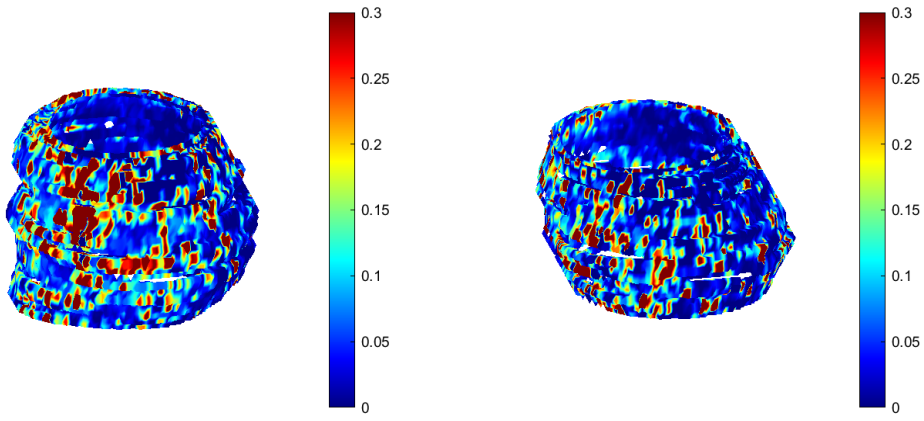

3D K_{trans} maps generated with DCE-net. The color scale represents the value of K_{trans} in min^{-1}.

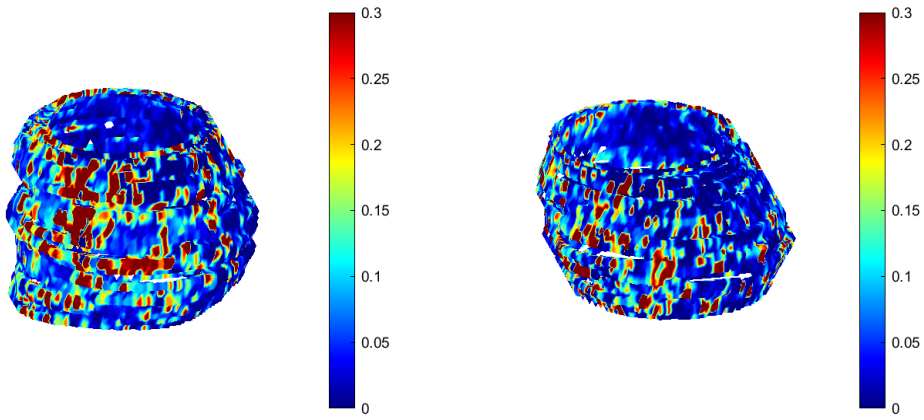

B.2 Patient 3

3D K_{trans} maps generated with LSQ fitting method. The color scale represents the value of K_{trans} in min^{-1}.

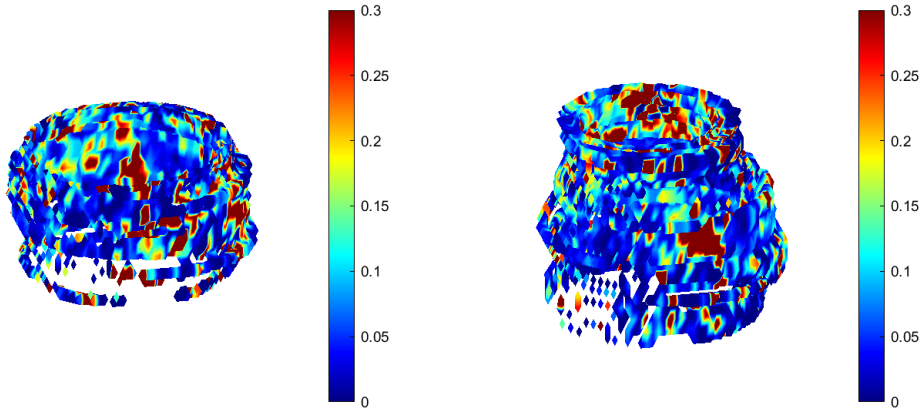

3D K_{trans} maps generated with DCE-net. The color scale represents the value of K_{trans} in min^{-1}.

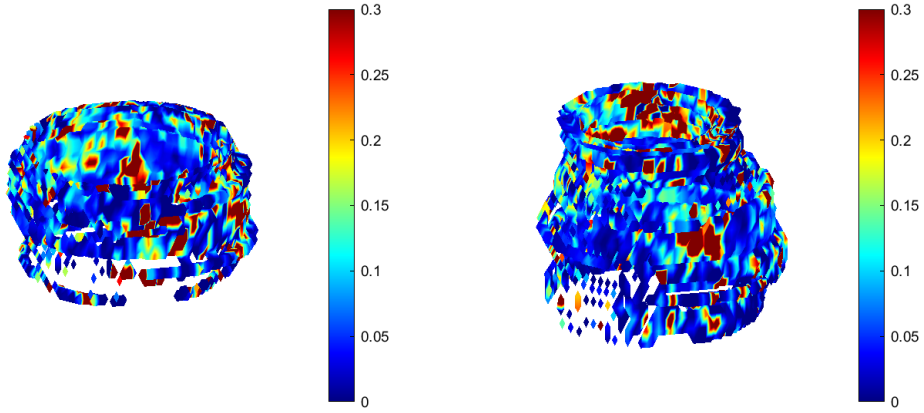

B.3 Patient 4

3D K_{trans} maps generated with LSQ fitting method. The color scale represents the value of K_{trans} in min^{-1}.

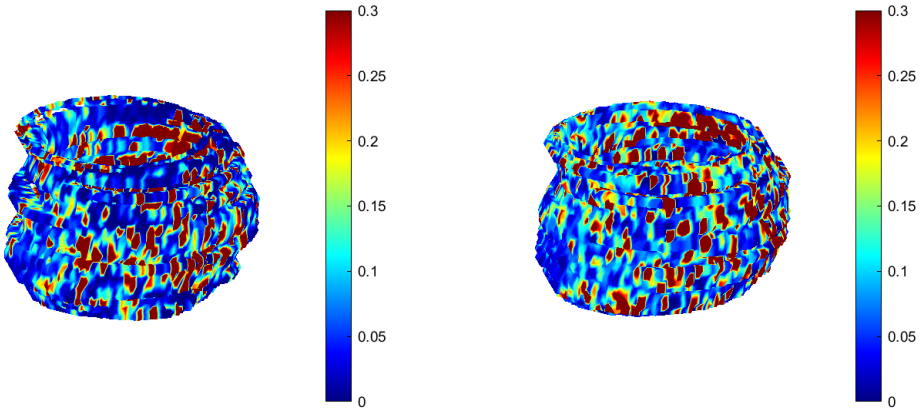

3D K_{trans} maps generated with DCE-net. The color scale represents the value of K_{trans} in min^{-1}.

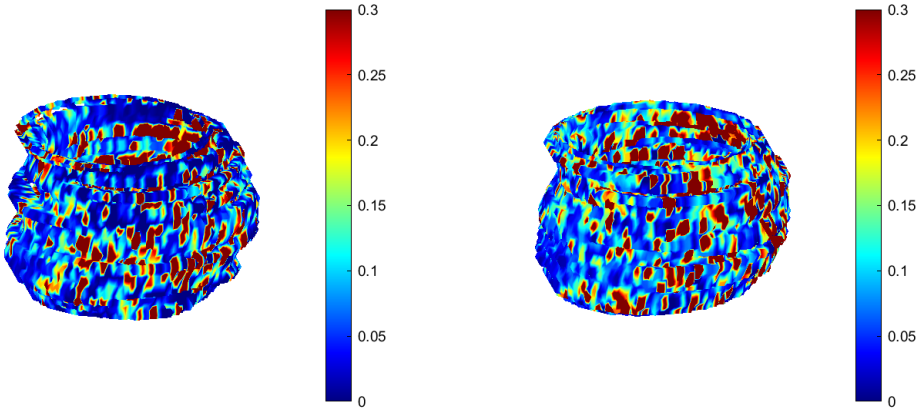

B.4 Patient 5

3D K_{trans} maps generated with LSQ fitting method. The color scale represents the value of K_{trans} in min^{-1}.

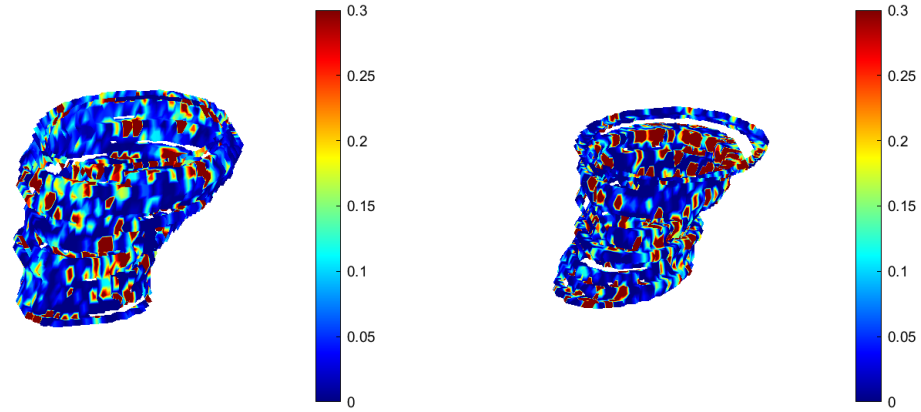

3D K_{trans} maps generated with DCE-net. The color scale represents the value of K_{trans} in min^{-1}.

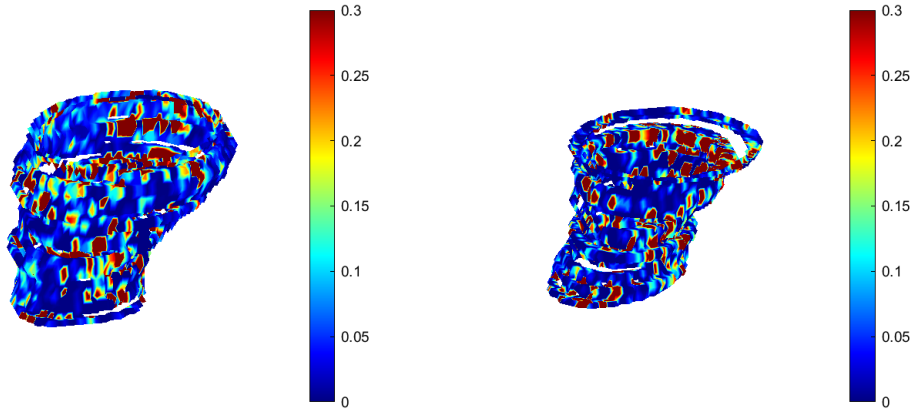

B.5 Patient 6

3D K_{trans} maps generated with LSQ fitting method. The color scale represents the value of K_{trans} in min^{-1}.

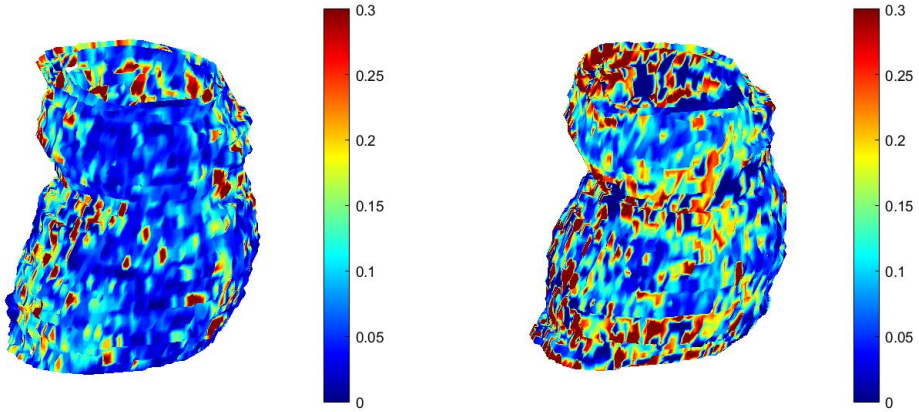

3D K_{trans} maps generated with DCE-net. The color scale represents the value of K_{trans} in min^{-1}.

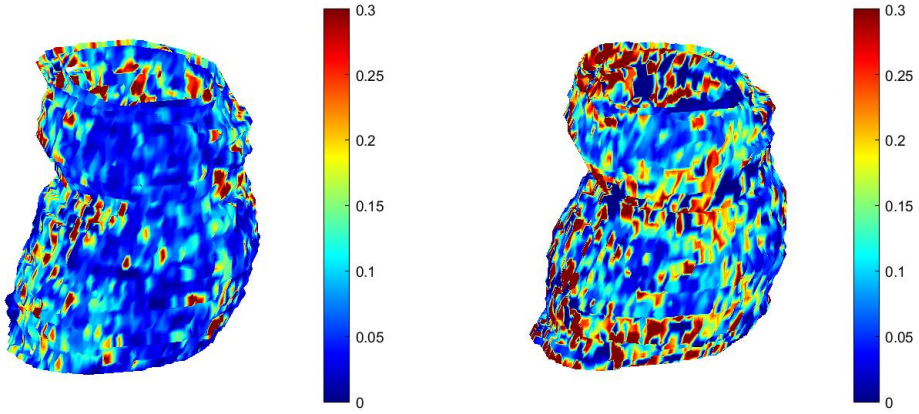

B.6 Patient 7

3D K_{trans} maps generated with LSQ fitting method. The color scale represents the value of K_{trans} in min^{-1}.

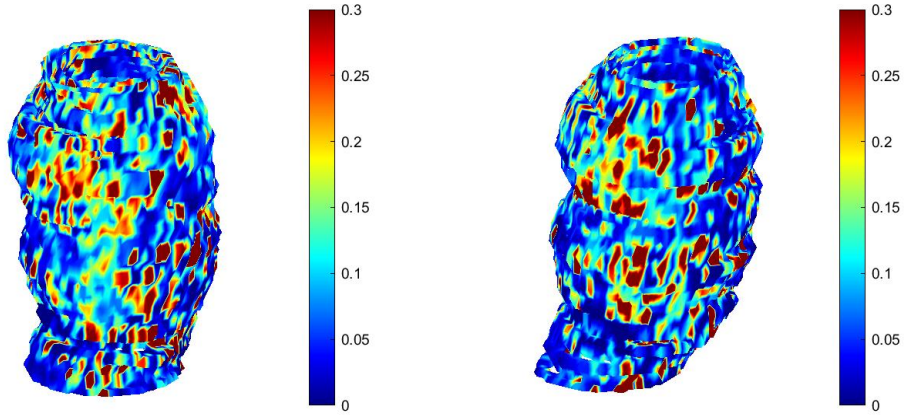

3D K_{trans} maps generated with DCE-net. The color scale represents the value of K_{trans} in min^{-1}.

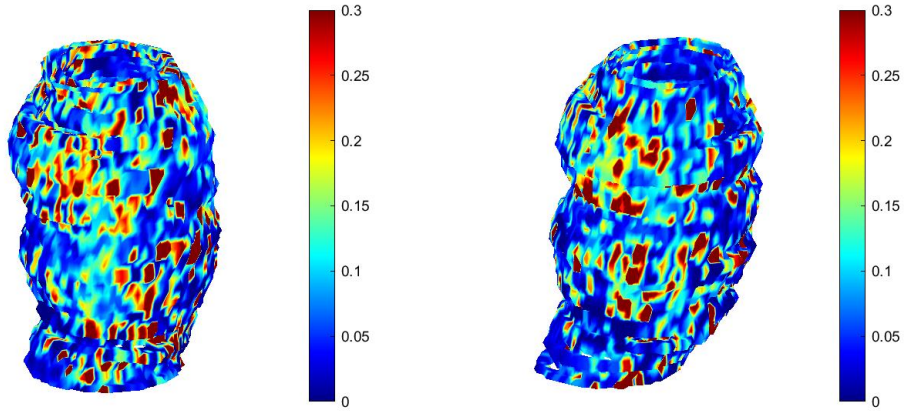

B.7 Patient 9

3D K_{trans} maps generated with LSQ fitting method. The color scale represents the value of K_{trans} in min^{-1}.

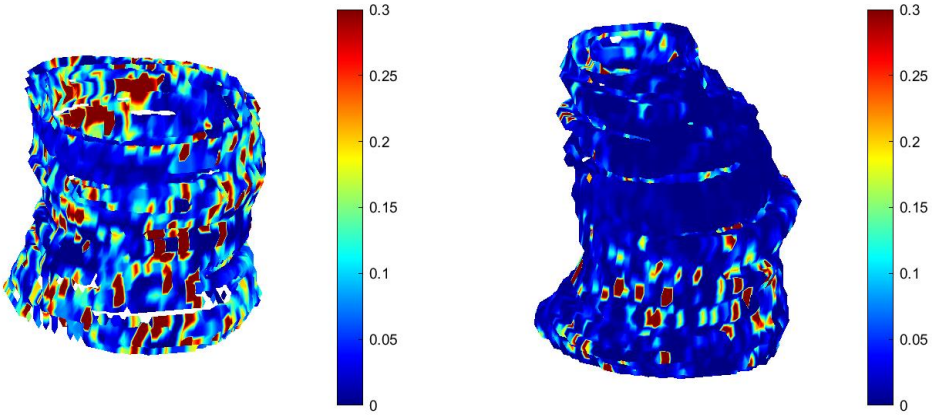

3D K_{trans} maps generated with DCE-net. The color scale represents the value of K_{trans} in min^{-1}.

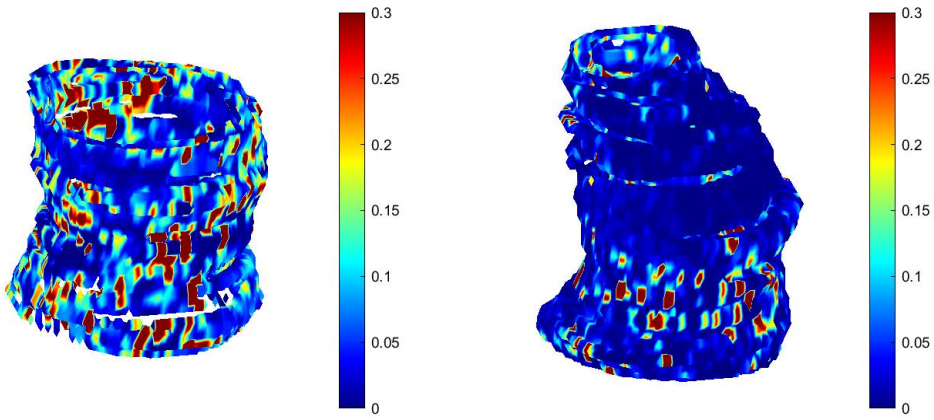

B.8 Patient 11

3D K_{trans} maps generated with LSQ fitting method. The color scale represents the value of K_{trans} in min^{-1}.

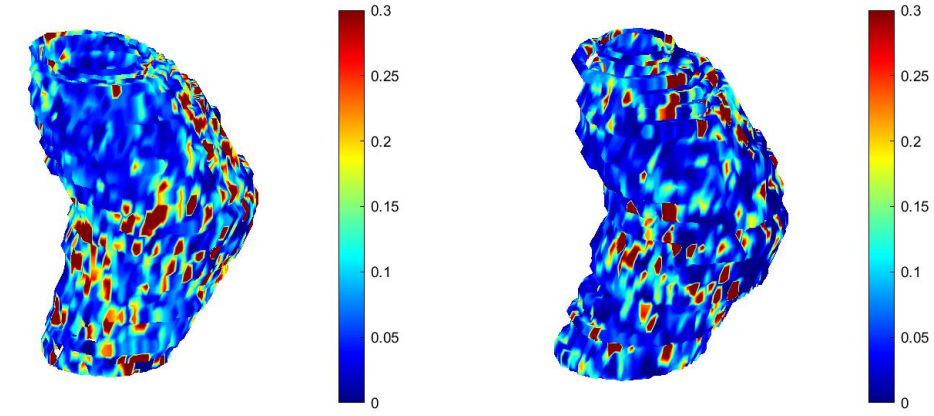

3D K_{trans} maps generated with DCE-net. The color scale represents the value of K_{trans} in min^{-1}.

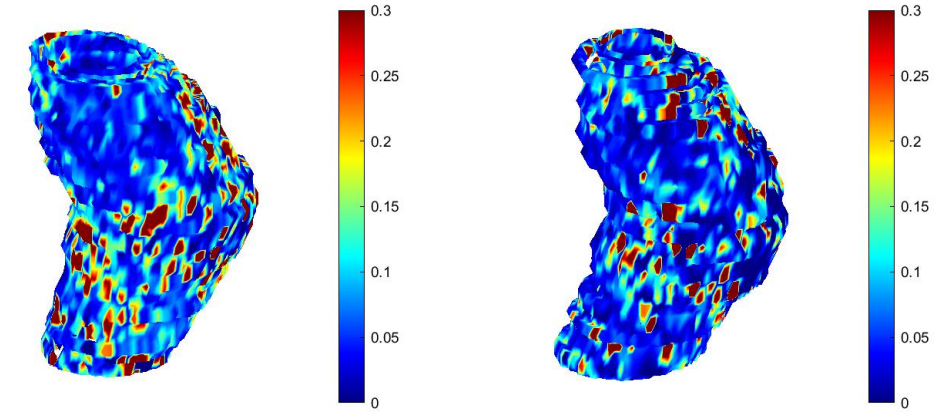

B.9 Patient 12

3D K_{trans} maps generated with LSQ fitting method. The color scale represents the value of K_{trans} in min^{-1}.

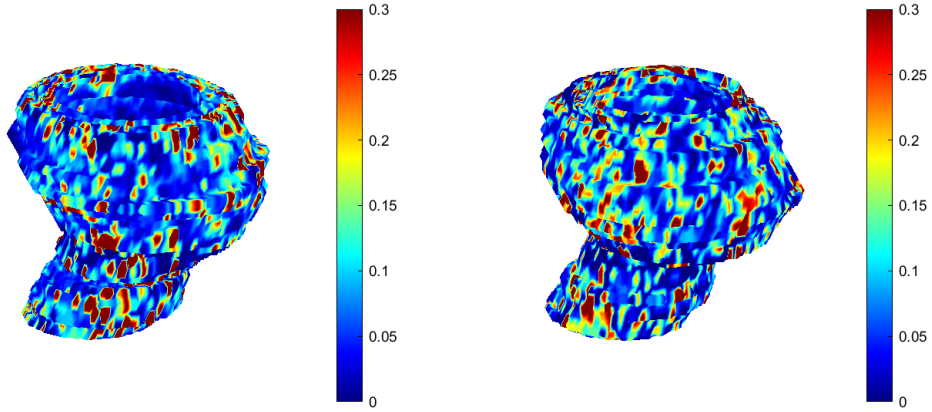

3D K_{trans} maps generated with DCE-net. The color scale represents the value of K_{trans} in min^{-1}.

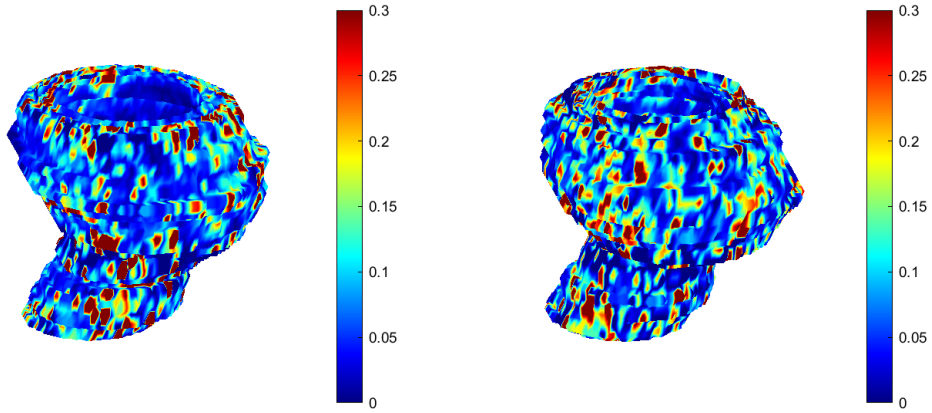

B.10 Patient 13

3D K_{trans} maps generated with LSQ fitting method. The color scale represents the value of K_{trans} in min^{-1}.

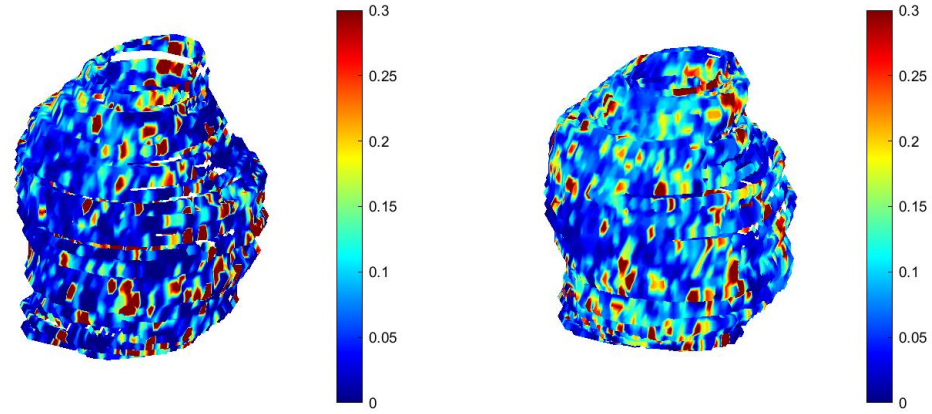

3D K_{trans} maps generated with DCE-net. The color scale represents the value of K_{trans} in min^{-1}.

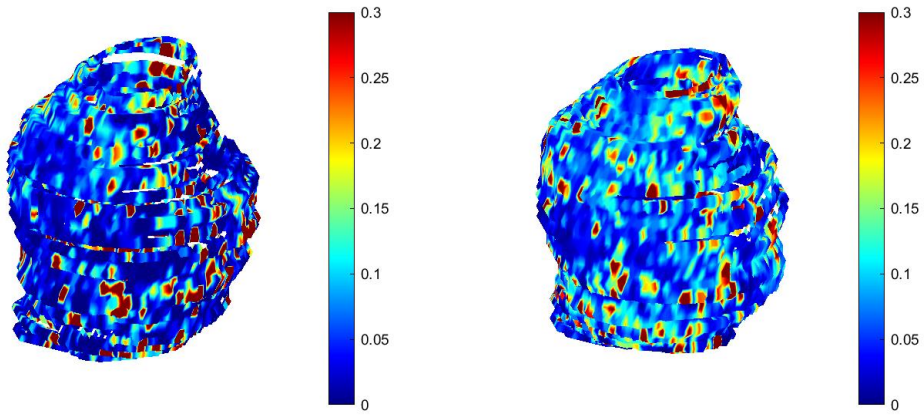

B.11 Patient 14

3D K_{trans} maps generated with LSQ fitting method. The color scale represents the value of K_{trans} in min^{-1}.

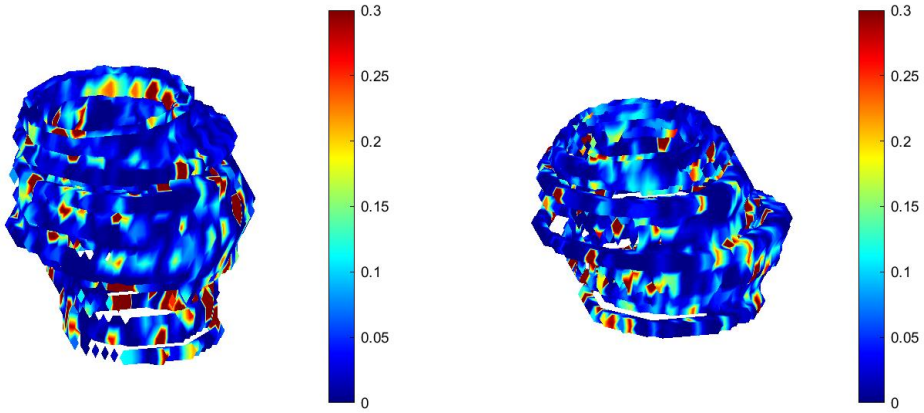

3D K_{trans} maps generated with DCE-net. The color scale represents the value of K_{trans} in min^{-1}.

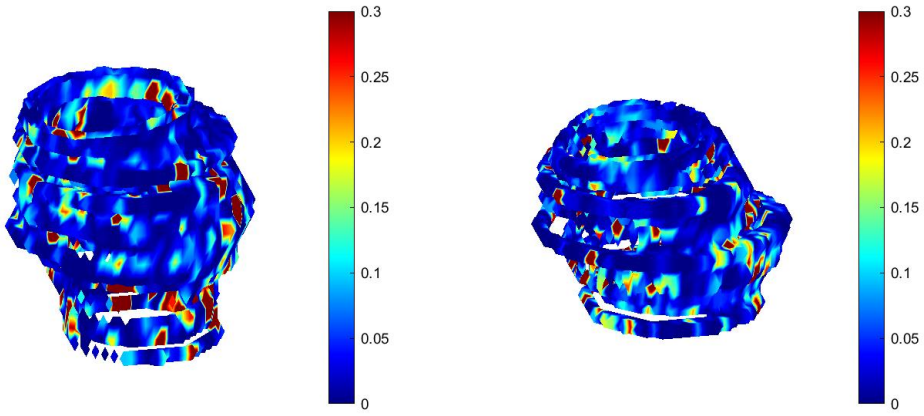

B.12 Patient 15

3D K_{trans} maps generated with LSQ fitting method. The color scale represents the value of K_{trans} in min^{-1}.

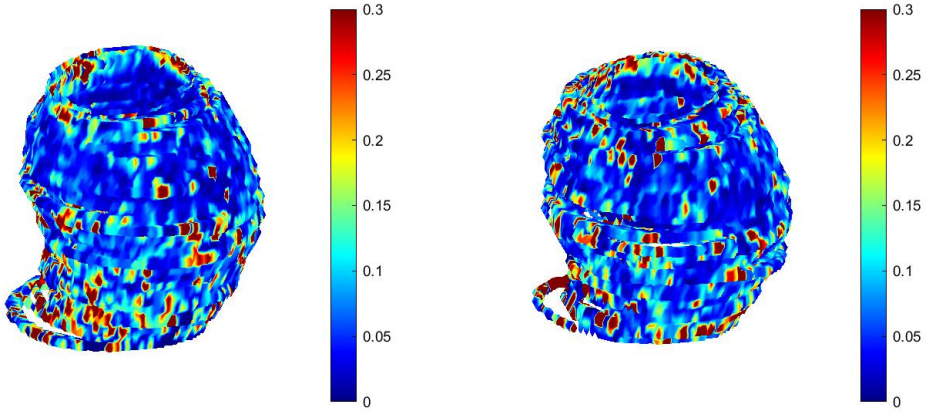

3D K_{trans} maps generated with DCE-net. The color scale represents the value of K_{trans} in min^{-1}.

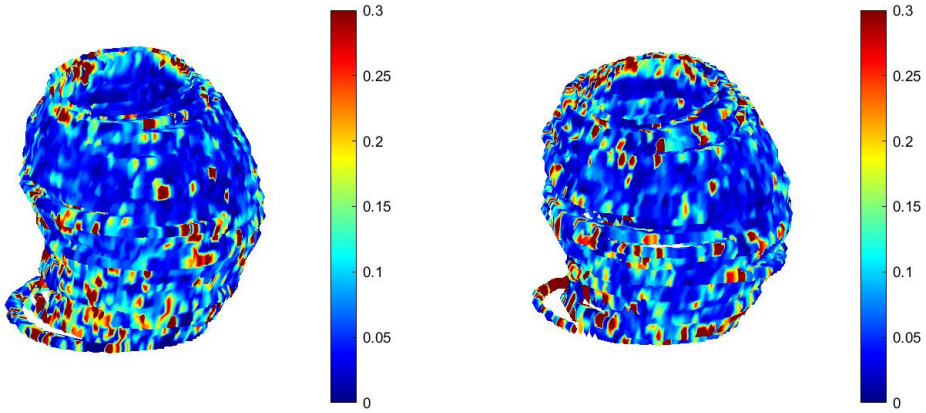

B.13 Patient 16

3D K_{trans} maps generated with LSQ fitting method. The color scale represents the value of K_{trans} in min^{-1}.

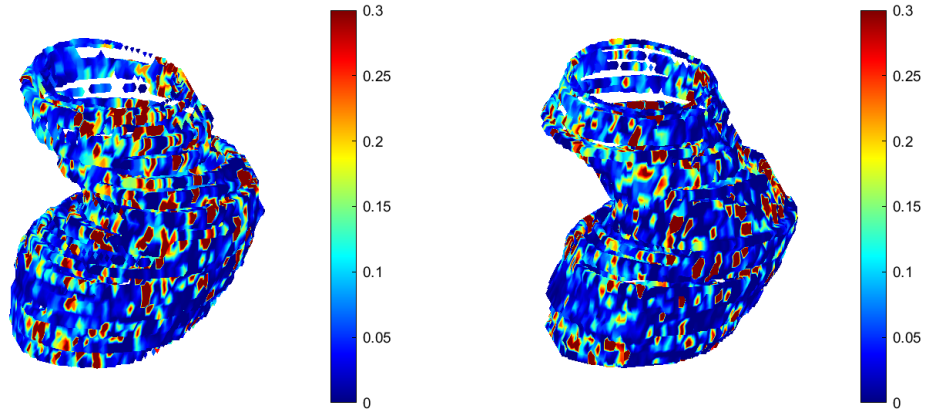

3D K_{trans} maps generated with DCE-net. The color scale represents the value of K_{trans} in min^{-1}.

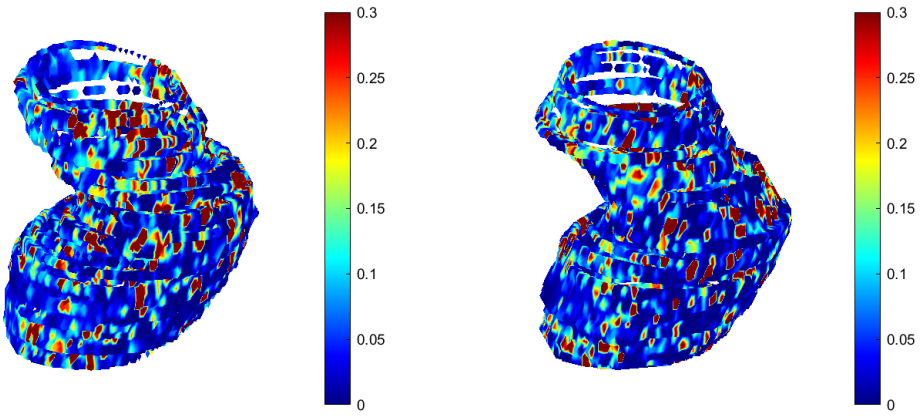

B.14 Patient 17

3D K_{trans} maps generated with LSQ fitting method. The color scale represents the value of K_{trans} in min^{-1}.

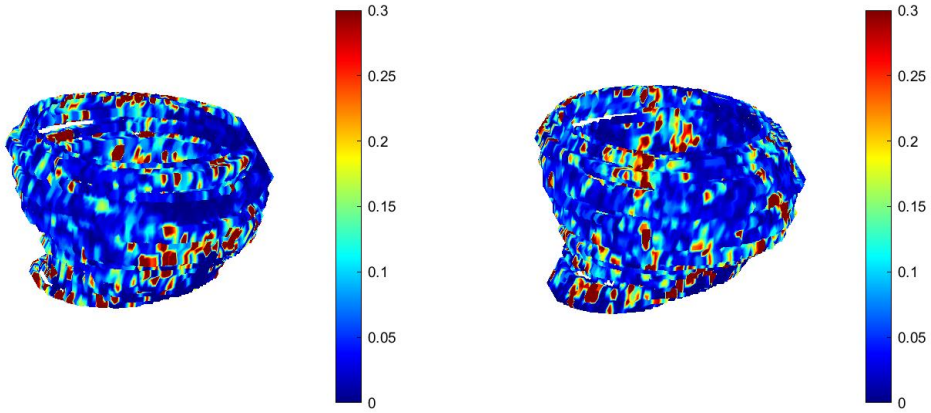

3D K_{trans} maps generated with DCE-net. The color scale represents the value of K_{trans} in min^{-1}.

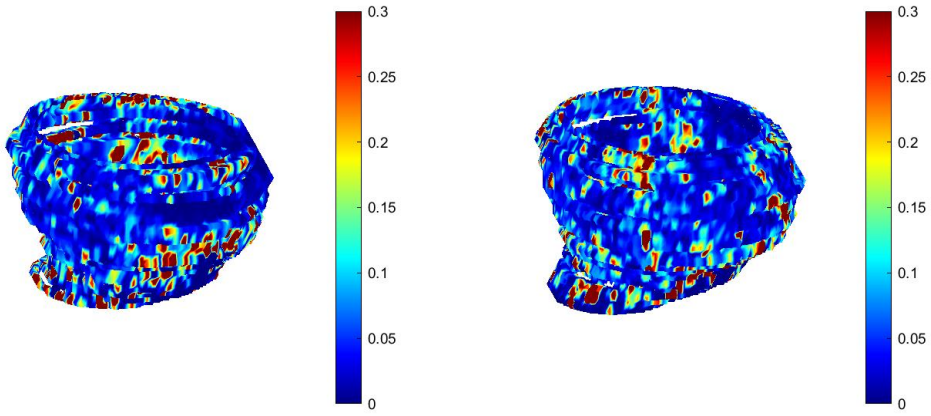

B.15 Patient 18

3D K_{trans} maps generated with LSQ fitting method. The color scale represents the value of K_{trans} in min^{-1}.

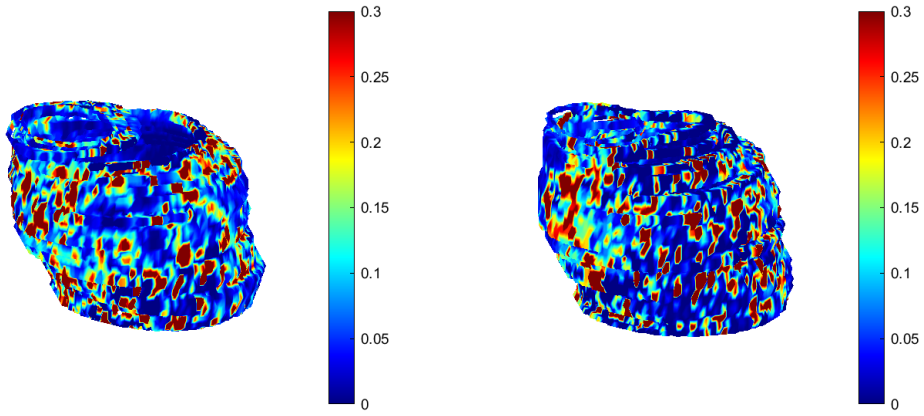

3D K_{trans} maps generated with DCE-net. The color scale represents the value of K_{trans} in min^{-1}.

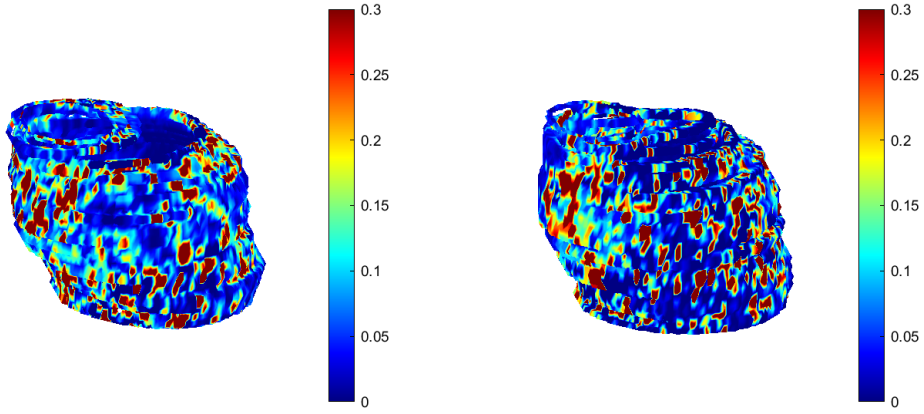

B.16 Patient 19

3D K_{trans} maps generated with LSQ fitting method. The color scale represents the value of K_{trans} in min^{-1}.

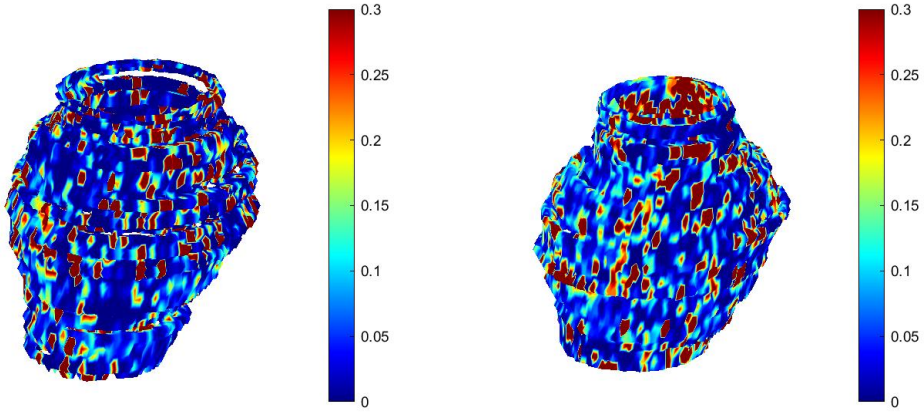

3D K_{trans} maps generated with DCE-net. The color scale represents the value of K_{trans} in min^{-1}.

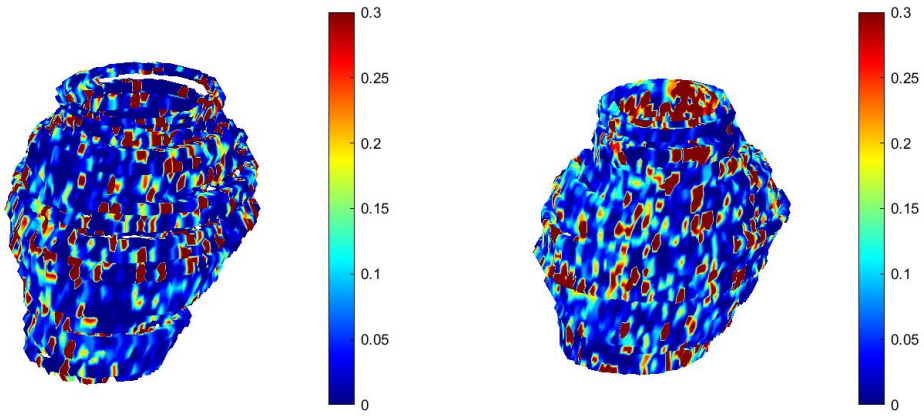

B.17 Patient 20

3D K_{trans} maps generated with LSQ fitting method. The color scale represents the value of K_{trans} in min^{-1}.

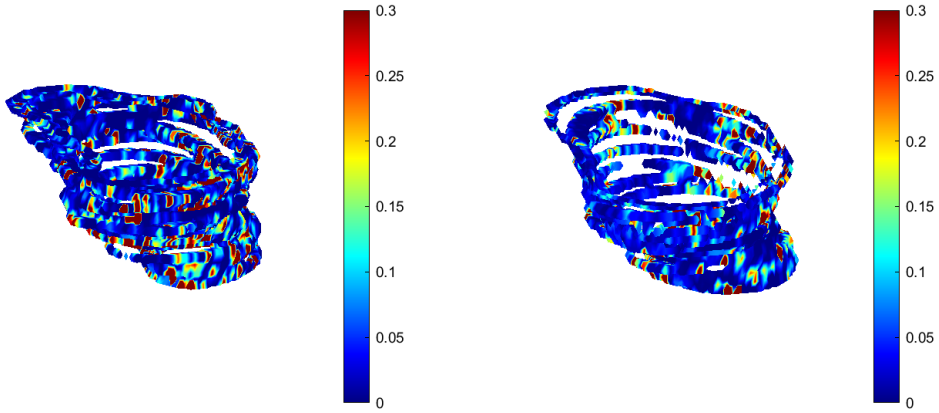

3D K_{trans} maps generated with DCE-net. The color scale represents the value of K_{trans} in min^{-1}.

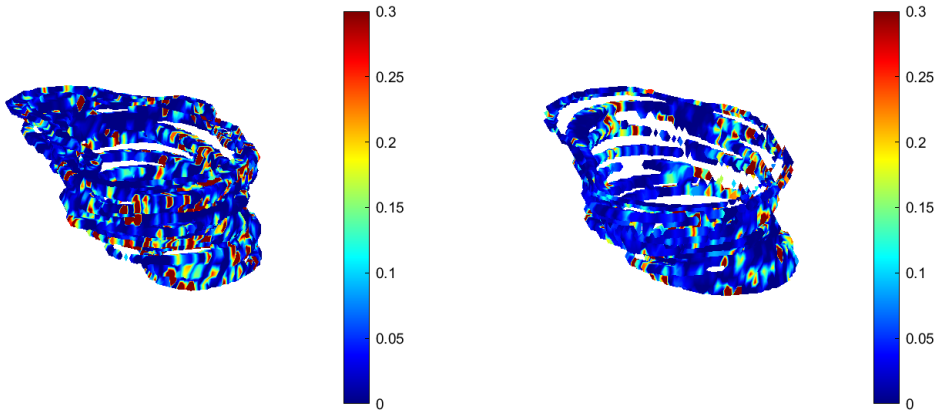

C Reproducibility K_{trans} maps

C.1 Reproducibility LSQ fitting for small segments for each patient separately

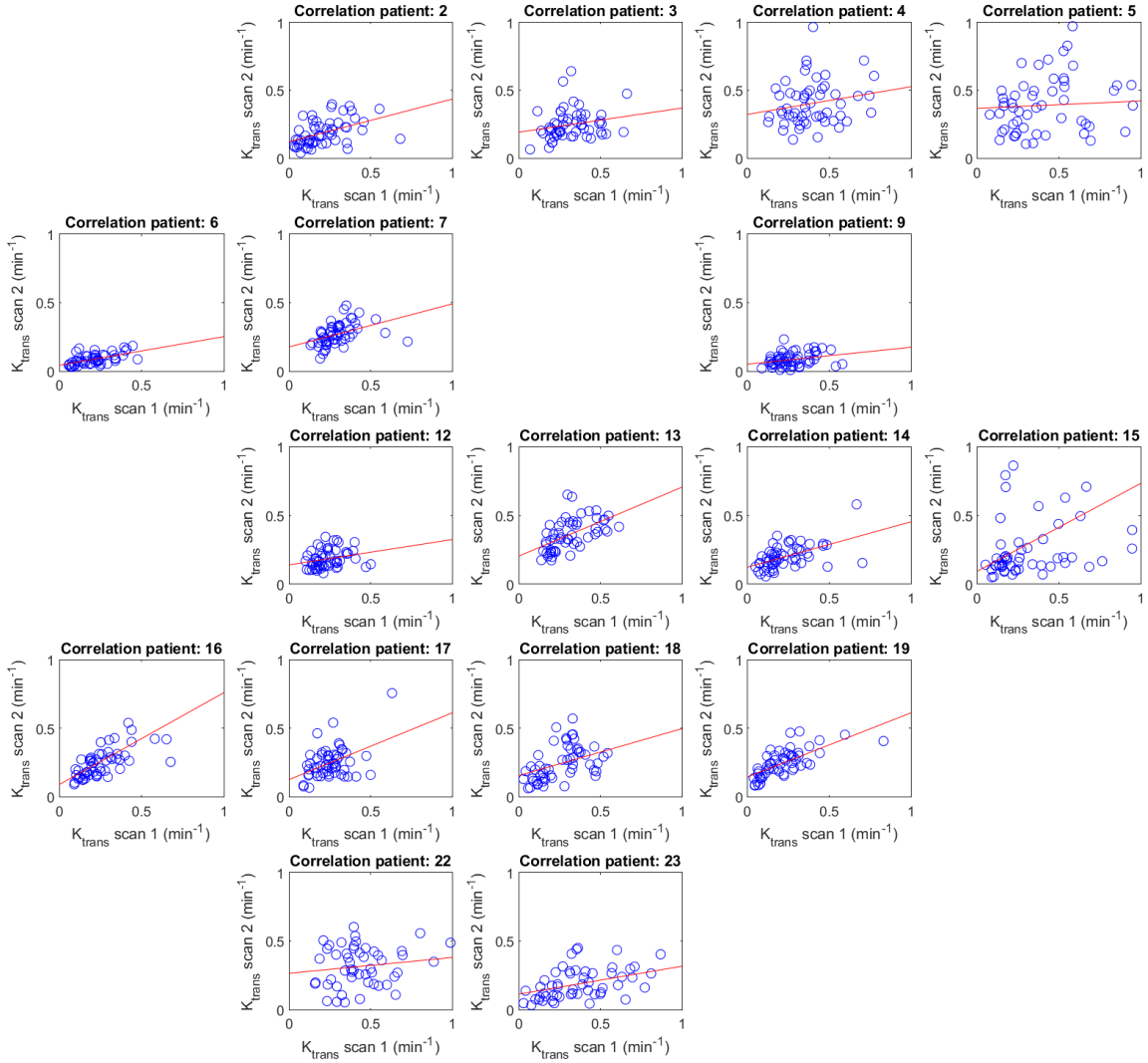

Figure C1. Correlation plots scan and rescan of all scanned patients for the LSQ fitting.

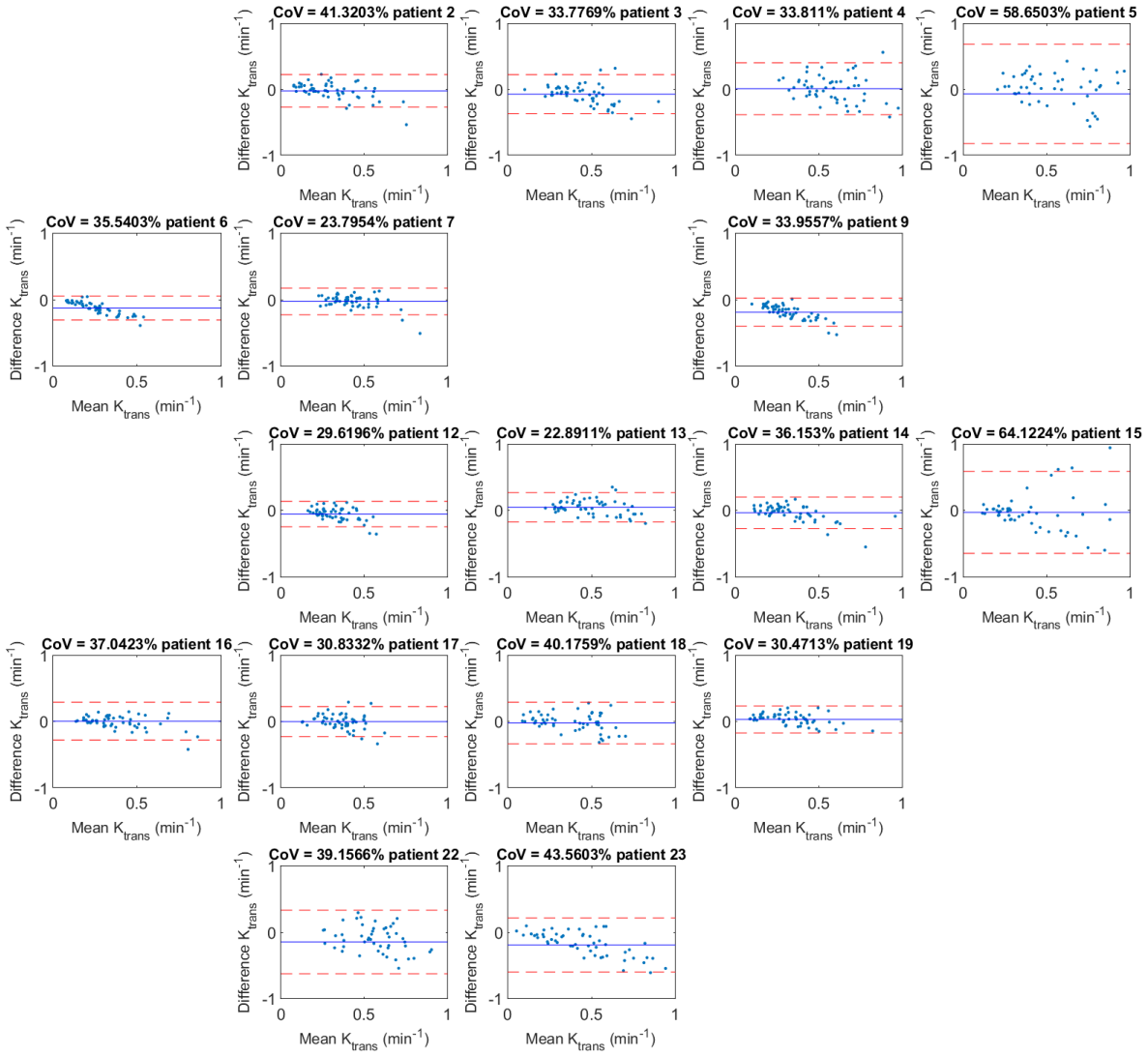

Figure C2. Bland-Atlman plots of scan and rescan of the LSQ fitting for all scanned patients, including the coefficient of variation (CoV).

C.2 Reproducibility DCE-net for small segments for each patient separately

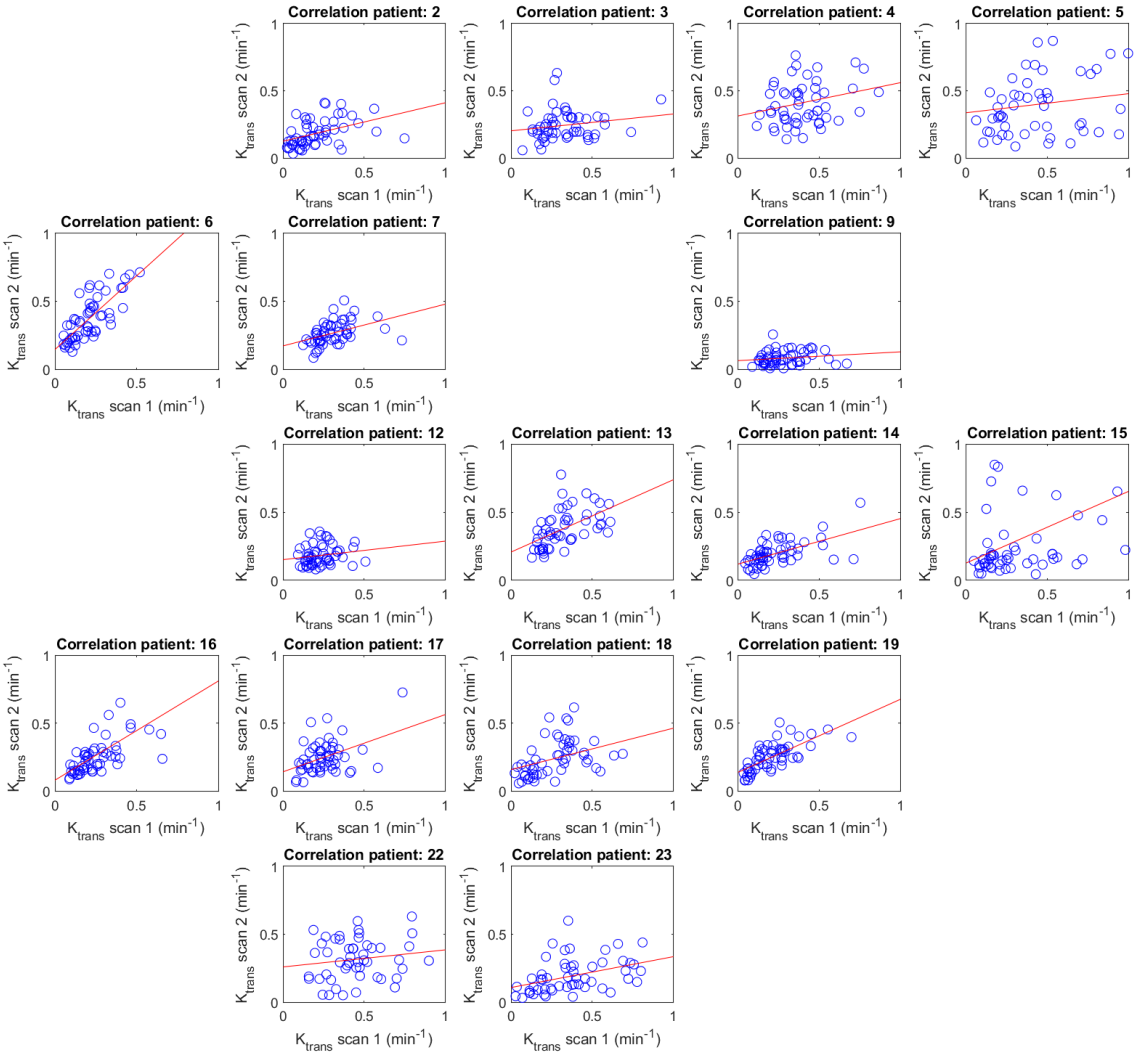

Figure C3. Correlation plots scan and rescan of all scanned patients for the DCE-net.

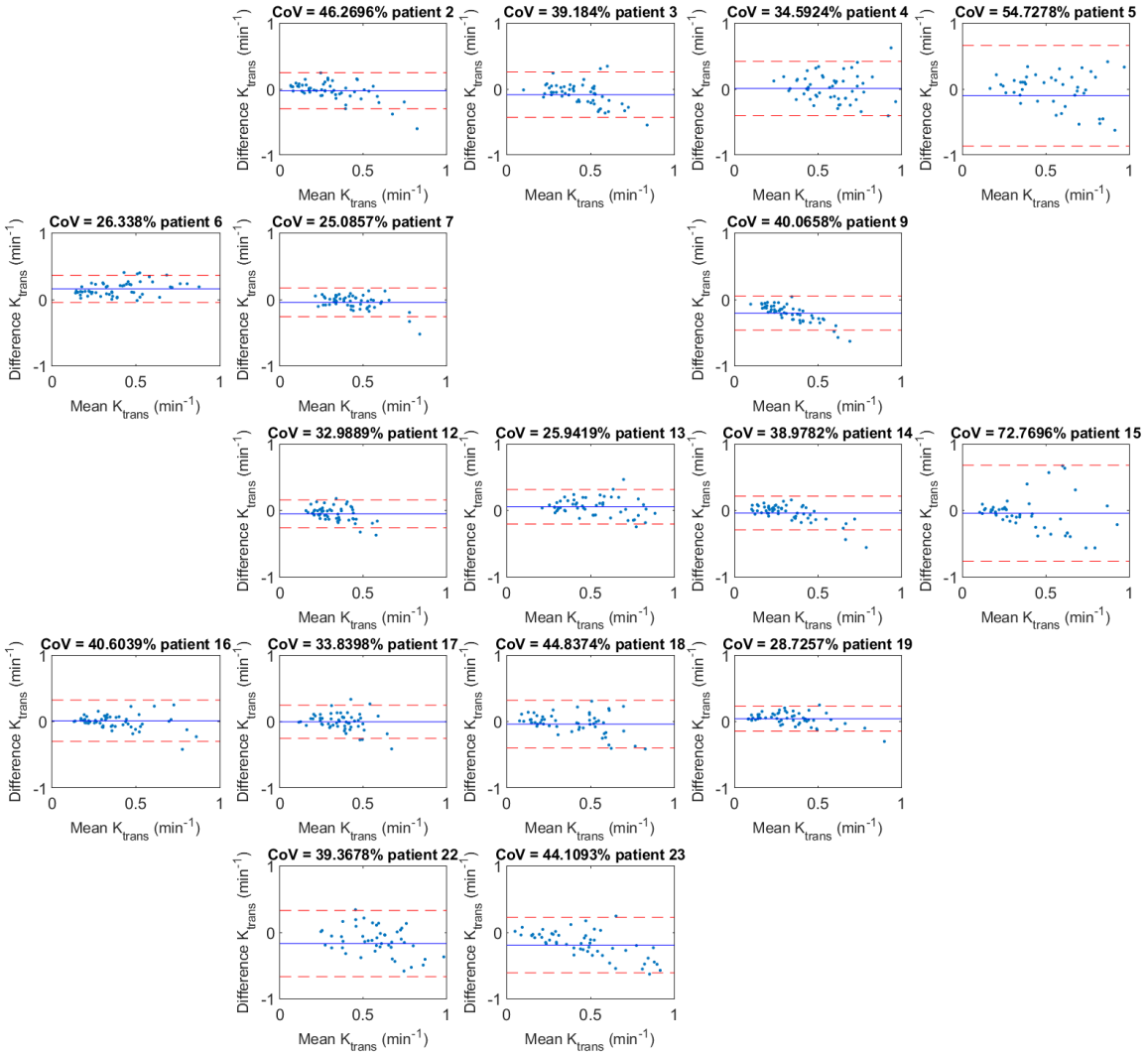

Figure C4. Bland-Atlman plots of scan and rescan of the DCE-net for all scanned patients, including the coefficient of variation (CoV)..

C.3 Reproducibility DCE-net for large segments

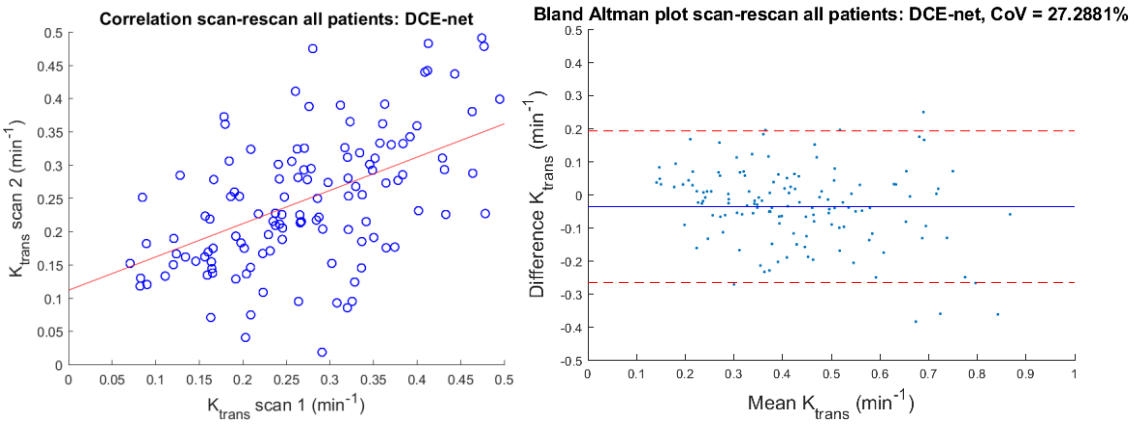

Figure C527. Bland-Altman plots of the larger segments for the DCE-net for all patients combined. Left: correlation plot of the first and second scan with the dots representing the median K_{trans} values of all large segments for all patients. Right: Bland-Altman plot with the blue dots representing the difference of the two K_{trans} values (first and second scan) for each larger segment on the vertical axis and the average of the two K_{trans} values on the horizontal axis. The blue line is the average difference and the red dotted lines are the standard deviation of the K_{trans} values.